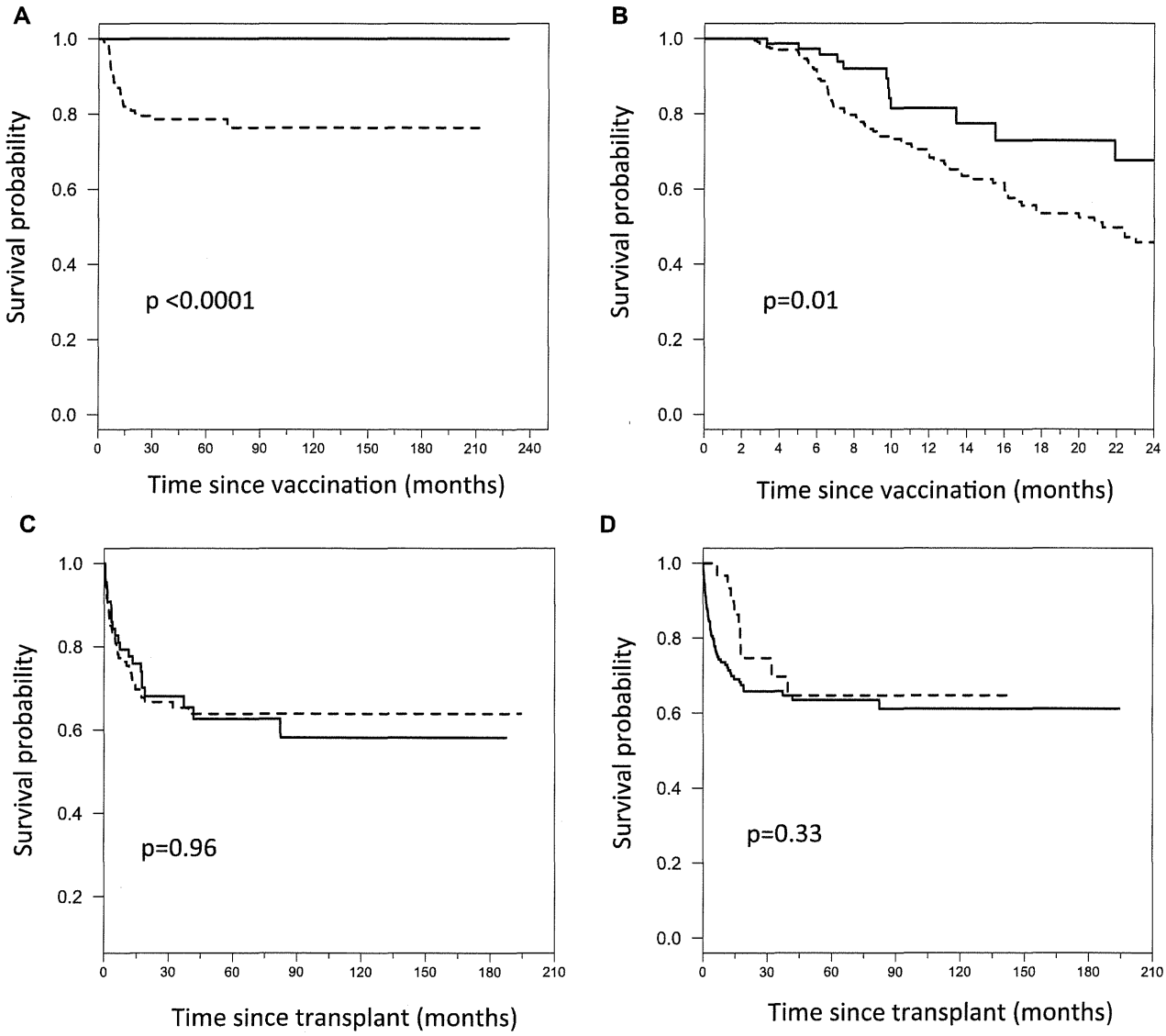

FIG 2. Time-to-event analysis by age at BCG vaccination and age at HSCT. **A,** Kaplan-Meier curves for the time from vaccination to death caused by BCG-associated complications comparing early (≤1 month of age, *dashed line*) versus late (>1 month of age, *solid line*) vaccination ($P < .0001$). **B,** Kaplan-Meier curves for the time from vaccination to death within 24 months of age before HSCT comparing early (≤1 month of age, *dashed line*) versus late (>1 month of age, *solid line*) vaccination ($P = .01$). **C,** Kaplan-Meier curves for time from HSCT to death comparing early (≤1 month of age, *dashed line*) versus late (>1 month of age, *solid line*) vaccination ($P = .96$). **D,** Kaplan-Meier curves for the time from HSCT to death comparing early (≤3 months of age, *dashed line*) versus late (>3 months of age, *solid line*) transplantation ($P = .33$).

BCG-associated complications were detected either among patients receiving matched related, matched unrelated, mismatched related, or mismatched unrelated forms of HSCT ($P = .97$). However, death caused by BCG-associated complications was still more frequent among patients receiving early vaccination compared with those vaccinated later ($P = .049$). Death caused by BCG-associated complications was also significantly more frequent among patients undergoing HSCT with localized or disseminated BCG-associated complications versus those with no manifestations ($P = .006$). When all-cause mortality was compared among patients receiving HSCT, no significant difference was detected between patients receiving early versus late BCG vaccination ($P = .96$), implying that after HSCT, the age at BCG vaccination has no significant effect on survival rates (Fig 2). Finally, although we did not find significant differences in post-HSCT survival between early (≤3 months) and late (>3 months) HSCT ($P = .33$), the difference between these 2 groups within the first 12 months after transplantation was statistically significant ($P = .01$, Fig 2).

Of 190 patients who underwent HSCT or another form of SCID treatment, 55 (29%) had IRS (33 with disseminated disease, 14 with localized complications, and 8 with no manifestations). Most patients (57%) presented with these manifestations within a month of HSCT. IRS prevalence was also analyzed in different

subsets of patients: those receiving antimycobacterial treatment while BCG asymptomatic had significantly less of this complication (5/64) compared with either BCG-symptomatic antimycobacterial-treated patients (33/81, $P < .0001$) or nontreated patients (17/45, $P = .0003$).

DISCUSSION

The prevalence of BCG-associated complications in the general population can vary widely depending on the reporting country and the vaccine strain used. However, reports of 1 in 2,500 vaccinees presenting with localized BCG-associated complications and 1 in 100,000 presenting with disseminated complications represent a fair estimate of the prevalence of such complications.[1,9] When focused exclusively on patients given a diagnosis of SCID, the prevalence of BCG-associated complications has been estimated to be higher than in the general population,[10-12] although a definitive effect has not previously been established.

The cumulative experience of 28 centers in 17 countries from Africa, the Americas, Asia, and Europe confirms that, as expected, BCG-associated complications are more prevalent in patients with SCID than in the general population. On the basis of our observations, one in every 2 BCG-vaccinated patients with SCID had BCG-associated manifestations, two thirds in the form of disseminated complications (an approximate 33,000-fold increased compared with the general population) and the other third in the form of localized complications (an approximate 400-fold increase). Our analysis found 2 individual variables to significantly correlate with this increased prevalence of BCG-associated complications: the total number of T cells at the time of SCID diagnosis and the patient's age at the time of BCG vaccination. Although patients with SCID presenting with higher T-cell numbers were underrepresented among those with BCG-associated complications, these results should be cautiously interpreted. Maternal T-cell engraftment was not systematically evaluated in most of the patients surveyed, and patients presenting with Omenn syndrome and oligoclonal T-cell expansion were not excluded from the analysis. Furthermore, detailed information on T-cell functional studies were not part of the original survey and analysis. On the other hand, age at BCG vaccination appeared to be a strong predictor for BCG-associated complications, with patients vaccinated within the first month of life having a substantially higher risk, which in turn was also associated with an increased rate of death caused by vaccine-associated complications. Age at BCG vaccination was independent of other variables, including BCG strain, vaccination route, or type of SCID diagnosed. Less clear than the association between age of vaccination and complications are the mechanism or mechanisms underlying this finding. All patients with SCID, independent of their underlying genetic defect, share a defective adaptive immune response. Therefore the relative maturity of the innate immune arm involved with controlling mycobacterial infections could by hypothesized as a factor altering the balance toward controlling or not controlling BCG.[13,14] Equally as relevant as determining the biological mechanism to explain this variability is developing a strategy to intervene and improve the clinical outcome.

BCG vaccine has a worldwide coverage of 88% (http://apps.who.int/immunization_monitoring/en/globalsummary/GS_GLOProfile.pdf?CFID=6942726&CFTOKEN=73185195), and most of these vaccines are applied at birth (http://www.bcgatlas.org/). Similar to other large SCID series published,[15,16] the majority of patients in our cohort (63%) were given diagnoses of SCID within the first 6 months of life. Until safer and more efficient forms of antituberculosis vaccines become available,[17] delaying BCG vaccination beyond 1 month of age is likely to have a favorable effect in this highly vulnerable population, as well as other susceptible neonates (eg, HIV-positive infants).[18] Moreover, delaying BCG vaccination would also benefit the clinical effect of neonatal SCID screening, preventing application of an absolutely contraindicated vaccine before establishing the diagnosis of SCID. This issue will become increasingly relevant as countries still encouraging early BCG vaccination start implementing neonatal SCID screening.[19,20]

However, 2 major drawbacks could be foreseen in delaying BCG vaccination: the "missed opportunity" of vaccinating patients after birth based on the concept that there will be an associated decrease in coverage and the potential increased risk of BCG-preventable diseases during the "unprotected" intervals. WHO data (updated to July 12, 2012) demonstrated a BCG coverage of 89.2% for countries encouraging at-birth vaccination policies, values that are very similar to the 89% coverage in the same countries for administration of the third dose of diphtheria-pertussis-tetanus vaccine (DPT3) typically given at 6 months of age (http://apps.who.int/immunization_monitoring/en/globalsummary/timeseries/tscoveragedtp3.htm). These data suggest there would be little or no decrease in coverage by delaying BCG vaccination. In addition, the incidence of BCG-preventable mycobacterial diseases within the first 6 months of life is extremely uncommon. Literature on pediatric tuberculous meningitis, a BCG vaccine–preventable disease, shows that the mean age of presentation for this life-threatening disease is 23 to 49 months, although a few cases have been described during the first 6 months of life, whereas the medians span from 12 to 24 months of age.[21-26] The prospect of modifying BCG vaccination policies will certainly warrant extensive discussions balancing the needs of both the immunocompetent general population and highly vulnerable immunodeficient patients.

As expected, the major intervention affecting survival in this cohort of BCG-vaccinated patients with SCID was providing immunologic reconstitution by means of HSCT. Interestingly, a subset of patients who did not receive any antimycobacterial treatment but underwent HSCT did not have any BCG-associated complications or IRS (27/190). This outcome might suggest that HSCT by itself could suffice as an anti-BCG treatment; however, other variables could have potentially influenced these results, including vaccine viability,[27] SCID genotype (13 undefined SCIDs, 7 MHC class II deficiency, 2 *IL2RG*, 1 *JAK3*, 1 Artemis *(DCLRE1C)*, 1 *PNP*, 1 *IL7RA*, and 1 Cernunnos *(NHEJ1)*; median T-cell numbers, 250/μL; median age at HSCT, 7 months), higher maturity of innate immunity, residual acquired immunity, or other unidentified disease modifiers.

We observed that patients with SCID started on antimycobacterial therapy while BCG-asymptomatic had significantly fewer BCG-associated complications before HSCT, as well as less IRS after HSCT and decreased mortality caused by BCG-associated complications. The rationale for this approach is to control an infection involving the known inoculation of 37,500 to 3,200,000 live mycobacteria in a highly susceptible host.[28] However, we recognize that our data do not provide definitive proof of benefit for pre-emptive antimycobacterial therapy because of

confounding factors associated with this type of retrospective study. Still, in the setting of commonly used prophylactic therapy in patients with SCID (eg, immunoglobulin replacement and antimicrobial agents), it seems entirely appropriate to consider early initiation of antimycobacterial therapy at the time of SCID diagnosis. If this strategy is chosen, it is less clear which antimycobacterial scheme would be most effective.

In summary, our data strongly suggest that in patients with SCID, early BCG vaccination and lower T-cell numbers at SCID diagnosis increase the probability of having BCG-associated complications. Furthermore, patients with SCID presenting with BCG-associated complications are at increased risk of dying because of this. Finally, the age at BCG vaccination had no significant influence on survival rates in patients with SCID who received HSCT.

We thank all the patients, their families, and the medical teams who took and take care of our patients. We also thank the IT Department of the Hospital Garrahan in Buenos Aires, Argentina, for generating a Web site for the survey, and Dr Klaus Warnatz for his help and support with the logistics of the survey.

Clinical implications: Delaying BCG vaccination until after 1 month of age should diminish BCG-associated complications in patients with SCID and should not adversely affect BCG-preventable disease.

REFERENCES

1. Plotkin SA, Orenstein WA, Offit PA. *Vaccines*. 6th ed. Edinburgh: Elsevier/Saunders; 2013.
2. Comstock GW. The International Tuberculosis Campaign: a pioneering venture in mass vaccination and research. Clin Infect Dis 1994;19:528-40.
3. Fine PE. Bacille Calmette-Guerin vaccines: a rough guide. Clin Infect Dis 1995; 20:11-4.
4. Buckley RH. Transplantation of hematopoietic stem cells in human severe combined immunodeficiency: longterm outcomes. Immunol Res 2011;49:25-43.
5. Al-Herz W, Bousfiha A, Casanova JL, Chapel H, Conley ME, Cunningham-Rundles C, et al. Primary immunodeficiency diseases: an update on the classification from the international union of immunological societies expert committee for primary immunodeficiency. Front Immunol 2011;2:54.
6. General recommendations on immunization—recommendations of the Advisory Committee on Immunization Practices (ACIP). MMWR Morb Mortal Wkly Rep 2011;60:1-64.
7. Talbot EA, Perkins MD, Silva SF, Frothingham R. Disseminated Bacille Calmette-Guerin disease after vaccination: case report and review. Clin Infect Dis 1997;24: 1139-46.
8. Gantzer A, Neven B, Picard C, Brousse N, Lortholary O, Fischer A, et al. Severe cutaneous bacillus Calmette-Guerin infection in immunocompromised children: the relevance of skin biopsy. J Cutan Pathol 2013;40:30-7.
9. Lotte A, Wasz-Hockert O, Poisson N, Engbaek H, Landmann H, Quast U, et al. Second IUATLD study on complications induced by intradermal BCG-vaccination. Bull Int Union Tuberc Lung Dis 1988;63:47-59.
10. Romanus V, Fasth A, Tordai P, Wiholm BE. Adverse reactions in healthy and immunocompromised children under six years of age vaccinated with the Danish BCG vaccine, strain Copenhagen 1331: implications for the vaccination policy in Sweden. Acta Paediatr 1993;82:1043-52.
11. Gonzalez B, Moreno S, Burdach R, Valenzuela MT, Henriquez A, Ramos MI, et al. Clinical presentation of Bacillus Calmette-Guerin infections in patients with immunodeficiency syndromes. Pediatr Infect Dis J 1989;8:201-6.
12. Yao CM, Han XH, Zhang YD, Zhang H, Jin YY, Cao RM, et al. Clinical characteristics and genetic profiles of 44 patients with severe combined immunodeficiency (SCID): report from Shanghai, China (2004-2011). J Clin Immunol 2013; 33:526-39.
13. Sharma AA, Jen R, Butler A, Lavoie PM. The developing human preterm neonatal immune system: a case for more research in this area. Clin Immunol 2012;145: 61-8.
14. Satwani P, Morris E, van de Ven C, Cairo MS. Dysregulation of expression of immunoregulatory and cytokine genes and its association with the immaturity in neonatal phagocytic and cellular immunity. Biol Neonate 2005;88:214-27.
15. Buckley RH, Schiff RI, Schiff SE, Markert ML, Williams LW, Harville TO, et al. Human severe combined immunodeficiency: genetic, phenotypic, and functional diversity in one hundred eight infants. J Pediatr 1997;130:378-87.
16. Gennery AR, Slatter MA, Grandin L, Taupin P, Cant AJ, Veys P, et al. Transplantation of hematopoietic stem cells and long-term survival for primary immunodeficiencies in Europe: entering a new century, do we do better? J Allergy Clin Immunol 2010;126:602-10, e601-11.
17. Parida SK, Kaufmann SH. Novel tuberculosis vaccines on the horizon. Curr Opin Immunol 2010;22:374-84.
18. Koppel A, Leonardo-Guerrero J, Rives S, Paniagua-Torres N, Sparrow C, Beck-Sague CM. Immune reconstitution inflammatory syndrome due to *Mycobacterium bovis* Bacillus Calmette-Guerin in infants receiving highly active antiretroviral therapy: a call for universal perinatal rapid HIV testing prior to administration of BCG immunization of neonates. J Trop Pediatr 2010;56:280-3.
19. **Chien Y-H, Chiang S-C, Chang K-L, Yu H-H, Lee W-I, Tsai L-P, et al. Incidence of severe combined immunodeficiency through newborn screening in a Chinese population. J Formosan Med Assoc [Epub ahead of print].**
20. Kanegae MPP, dos Santos AMN, Cavalcanti CM, Condino Neto A. Newborn screening for severe combined immunodeficiency. Rev Brasil Alerg Imunopatol 2011;34:1-7.
21. van Well GT, Paes BF, Terwee CB, Springer P, Roord JJ, Donald PR, et al. Twenty years of pediatric tuberculous meningitis: a retrospective cohort study in the western cape of South Africa. Pediatrics 2009;123:e1-8.
22. Lee LV. Neurotuberculosis among Filipino children: an 11 years experience at the Philippine Children's Medical Center. Brain Dev 2000;22:469-74.
23. Farinha NJ, Razali KA, Holzel H, Morgan G, Novelli VM. Tuberculosis of the central nervous system in children: a 20-year survey. J Infect 2000;41:61-8.
24. Yaramis A, Gurkan F, Elevli M, Soker M, Haspolat K, Kirbas G, et al. Central nervous system tuberculosis in children: a review of 214 cases. Pediatrics 1998;102: E49.
25. Doerr CA, Starke JR, Ong LT. Clinical and public health aspects of tuberculous meningitis in children. J Pediatr 1995;127:27-33.
26. Paganini H, Gonzalez F, Santander C, Casimir L, Berberian G, Rosanova MT. Tuberculous meningitis in children: clinical features and outcome in 40 cases. Scand J Infect Dis 2000;32:41-5.
27. Ho MM, Markey K, Rigsby P, Jensen SE, Gairola S, Seki M, et al. Report of an international collaborative study to establish the suitability of using modified ATP assay for viable count of BCG vaccine. Vaccine 2008;26:4754-7.
28. Milstien JB, Gibson JJ. Quality control of BCG vaccine by WHO: a review of factors that may influence vaccine effectiveness and safety. B World Health Organ 1990;68:93-108.

SCIENTIFIC REPORTS

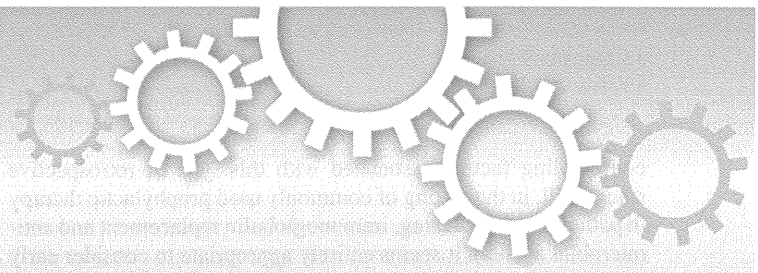

OPEN

SUBJECT AREAS:
CELL DEATH AND IMMUNE RESPONSE
LAB-ON-A-CHIP
SINGLE-CELL IMAGING
CELLULAR IMAGING

Received
3 October 2013

Accepted
2 April 2014

Published
22 April 2014

Correspondence and requests for materials should be addressed to O.O. (oosamu@rcai.riken.jp)

Real-time single-cell imaging of protein secretion

Yoshitaka Shirasaki[1], Mai Yamagishi[1], Nobutake Suzuki[1], Kazushi Izawa[2], Asahi Nakahara[3], Jun Mizuno[3], Shuichi Shoji[3], Toshio Heike[2], Yoshie Harada[4], Ryuta Nishikomori[2] & Osamu Ohara[1,5]

[1]RIKEN Center for Integrative Medical Sciences (IMS-RCAI), 1-7-22 Suehiro-cho Tsurumi-ku, Yokohama, Kanagawa 230-0045, Japan, [2]Department of Pediatrics, Kyoto University Graduate School of Medicine, 54 Shogoin-Kawahara-cho Sakyo-ku, Kyoto 606-8507, Japan, [3]Faculty of Science and Engineering, Waseda University, Okubo 3-4-1, Shinjuku, Tokyo 169-8555, Japan, [4]Institute for Integrated Cell-Material Sciences (WPI-iCeMS), Kyoto University Graduate School of Biostudies, Yoshida-Honmachi, Sakyo-ku, Kyoto 606-8501, Japan, [5]Department of Human Genome Research, Kazusa DNA Research Institute, 2-6-7 Kazusa-Kamatari, Kisarazu, Chiba 292-0818, Japan.

Protein secretion, a key intercellular event for transducing cellular signals, is thought to be strictly regulated. However, secretion dynamics at the single-cell level have not yet been clarified because intercellular heterogeneity results in an averaging response from the bulk cell population. To address this issue, we developed a novel assay platform for real-time imaging of protein secretion at single-cell resolution by a sandwich immunoassay monitored by total internal reflection microscopy in sub-nanolitre-sized microwell arrays. Real-time secretion imaging on the platform at 1-min time intervals allowed successful detection of the heterogeneous onset time of nonclassical IL-1β secretion from monocytes after external stimulation. The platform also helped in elucidating the chronological relationship between loss of membrane integrity and IL-1β secretion. The study results indicate that this unique monitoring platform will serve as a new and powerful tool for analysing protein secretion dynamics with simultaneous monitoring of intracellular events by live-cell imaging.

Many secreted proteins have been identified as important functional mediators of intercellular communication for the purpose of initiating various cellular processes, including differentiation and migration[1–3]. Cytokines in particular are one of the best studied classes of secreted proteins with broad effects on immune responses[4]. For the proper functioning of the immune system, cytokine synthesis and secretion must be tightly regulated, both spatially and temporally[5]. However, recent investigations using single-cell analysis have shown that immune cells display highly heterogeneous levels of cytokine secretion, even in cells with apparently similar phenotypes[6]. Therefore, the relationship between heterogeneous cytokine secretion at the single-cell level and the maintenance of homeostasis of the immune system has become a primary subject of investigation in the field of immunology. To address this issue, a methodology is required that enables delineation of spatiotemporal heterogeneity of cytokine secretion at the single-cell level. We have particularly focused on cytokine induction processes that occur in single cells induced by external stimulation, specifically with regard to (1) cellular heterogeneity in protein secretion dynamics and (2) the chronological relationship between intracellular event(s) and protein secretion. However, the technology available for monitoring protein secretion from single cells remains in its infancy.

Several groups have reported population analysis of cytokine secretion from single cells by using antibody-based immunoassay applications. Love *et al.* generated a secretion profile for a large collection of single cells by using microengraving[7] and succeeded in measuring the time course of cytokine secretion during T-lymphocyte maturation every 2 h for a period spanning several hours[8]. While these methods are efficient for their high throughput and/or the quantitative data generated, several challenges remain because of their inherent measurement limitations. In these methods, the accumulated cytokine molecules situated on a solid surface are labelled with a detection probe and are quantified after intensive wash steps, which are required to remove excess probe. Although this wash step, known as bound/free (B/F) separation, determines the signal/noise ratio for detection, this step also causes a lag between secretion and detection. Therefore, these methods cannot currently offer either a time interval of shorter than a few hours nor simultaneous real-time monitoring of a second intracellular variable (e.g. cell viability) over time.

Previously, our group and Salehi-Reyhani *et al.* respectively have successfully addressed this B/F separation issue in fluorescence immunoassays (FIAs) by taking advantage of near-field excitation in total internal reflection

fluorescence microscopy (TIRFM)[9,10]. In these studies, target proteins in each single-cell lysate segmented by microwells were quantified by detecting formation of immunocomplexes on the microwell bottom. In the current study, we have developed a novel assay platform for real-time monitoring of live single-cell cytokine secretion (Fig. 1). Each single cell is deposited on a microfabricated-well array (MWA) chip, which restricts cell migration as well as compartmentalizes the secretory signals from individual cells. The anti-cytokine capture antibody immobilized on the microwell bottom immediately captures the cytokine secreted from a cell, which enables TIRFM-FIA to function *in situ*. An MWA chip of the platform has an open architecture at the top of each microwell to permit easy access for stimulus delivery and to maintain culture conditions similar to those of a bulk experiment.

We characterized our secretion assay platform using a MWA chip consisting of glass and polydimethylsiloxiane (PDMS) in a quantitative manner by model experiments, introducing minute amounts of cytokine into microwells to mimic the milieu of cytokine secretion from a single cell. The platform was applied to monitor cytokine secretion from human peripheral blood monocytes at 1-min time intervals. We examined the IL-1β secretion process while simultaneously observing membrane integrity to determine the intracellular processes that occur at the time of cytokine secretion, since the mechanism underlying the non-classical IL-1β secretion pathway currently remains unclear.

Results

Characterization of an assay platform for real-time secretion imaging in an MWA chip. In this study, we designed a real-time single-cell imaging platform to monitor the secretion processes over time. We fabricated a novel MWA chip consisting of a PDMS well wall and a glass well bottom (see Supplementary Fig. S1a online). An objective of numerical aperture 1.49 was used to avoid the stray light due to the higher refractive index of PDMS (n = 1.42, Sylgard®184, Dow Corning Co., http://www1.dowcorning.com/DataFiles/090007c8803bb6a1.pdf) than that of medium (n = 1.34; Supplementary Fig. S1b–d). To assess restriction of the horizontal movement of secreted cytokine molecules by the microwell structure, we compared the decrease of fluorescently labelled protein from an observation area for TIRFM with and without microwell structures. The microwell structure slowed the escape of fluorescent molecules by about 20-fold (see Supplementary Fig. S2).

Next, to assess the functionality of time-resolved FIA (even in the open MWA), we introduced a miniscule amount of cytokine into microwells by using a microinjector to mimic cytokine secretion from a single cell (Fig. 2a). Fluorescence signals began to increase immediately after pulsed injection of IL-1β (time = 0; Fig. 2b, c) and increased without apparent change in localization over time (Fig. 2b), indicating that most of the injected IL-1β was instantly captured by antibody on the MWA bottom before diffusion throughout the microwell. From a separate experiment, we found that the fluorescence signals after the injection of pre-formed IL-1β-detection antibody complexes increased 15 times faster than that after the injection of IL-1β alone, suggesting that the released IL-1β rapidly bound to the capture antibodies on the bottom surface of the MWA chip (Fig. S3a, b). Therefore, binding of the detection antibody to form sandwich immunocomplexes was likely the rate-limiting step for the increase in the fluorescence signals under the experimental conditions employed. Once the immunocomplex was formed, its dissociation occurred very slowly (dissociation constant $k_{off} < 2 \times 10^{-6}$ s^{-1}, Fig. S3c).

The rising curves of the fluorescence signal obtained from IL-1β injection were fitted with a single exponential, especially during

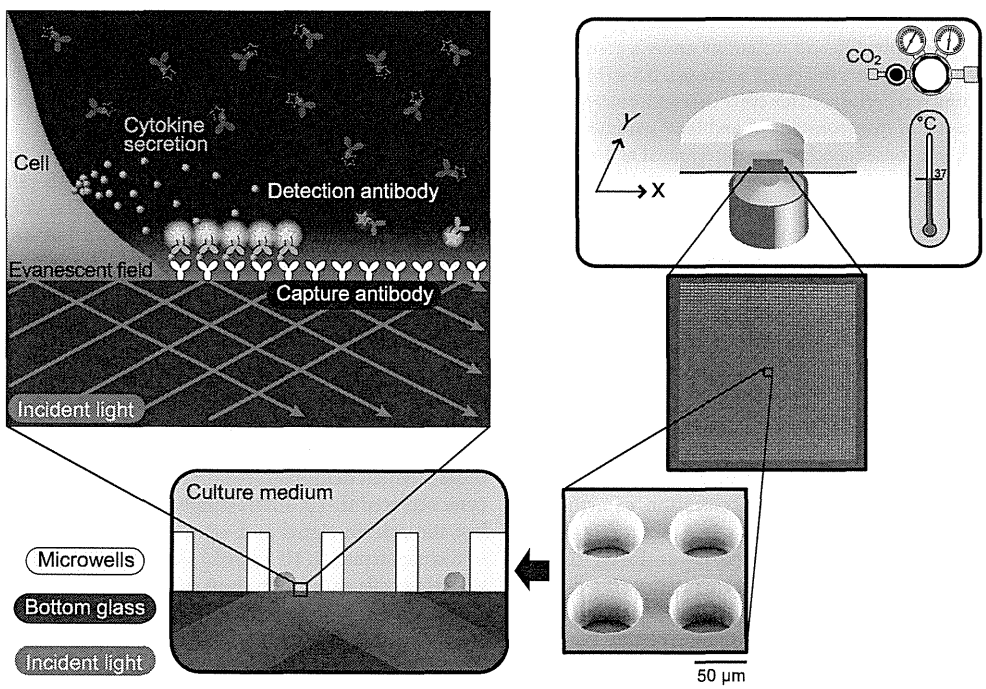

Figure 1 | Concept of the real-time single cell secretion assay platform. The schematic illustrates the concept of the platform for the real-time single cell secretion assay. The platform works with micro-fabricated well-array chip on a fully automated fluorescence microscopy. The platform maintains the environment (temperature, concentration of CO_2, and humidity) of the chip. The chip has an array of nanolitre-sized microwells with a glass bottom, into which individual cells were introduced separately. The well has open-ended structure; therefore, culture medium was exchanged constantly during the observation. The anti-cytokine capture antibody was immobilized on the well bottom, onto which secreted cytokine and fluorescently labelled detection antibody were bound to form a sandwich immunocomplex. Near-field excitation by total internal reflection enabled selective detection of the cytokine sandwich immunocomplex immediately following secretion without the requirement for wash steps.

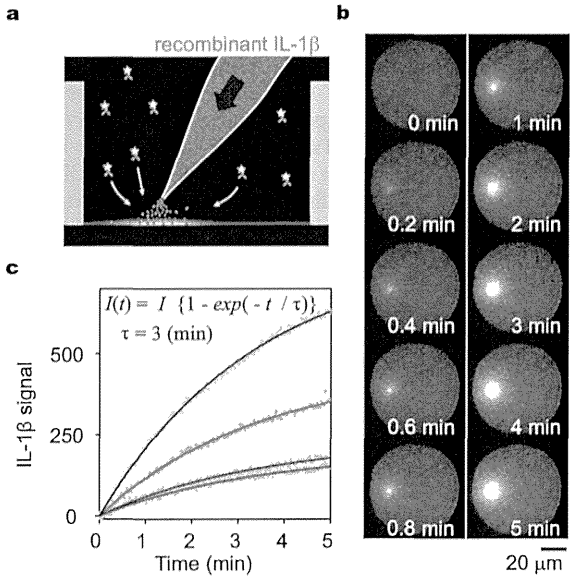

Figure 2 | Performance evaluation of time-resolved FIA in the MWA on model experiments using a microinjector. (a) Schema of the model experiment using pulsed injection of IL-1β via a microinjector. An increase in fluorescence signal was observed after pulse injecting 100 ng/mL of recombinant IL-1β into a microwell that was filled with the detection medium containing 30 nM fluorescently labelled detection antibody. (b) Representative images of developing fluorescence signals obtained from time-resolved FIA after introducing recombinant IL-1β into the microwell. Images were acquired once every second applying a 60-ms exposure time. The time elapsed after the pulsed injection is shown on each image. (c) Time course of the average intensity of the IL-1β signal in a microwell. Each dot denotes a measured value and solid lines denote fitted curves. Different colours denote different durations under a constant pressure of injection (1,200 Pa): 4 s (black), 2 s (green), 0.5 s (blue), and 0.1 s (cyan). Curve fitting was performed for every dataset from 0 to 5 min using the global parameter of time constant, τ, and local parameters of maximum intensity, I, and consequently τ was determined as 3 min.

5 min after injection, and the time constant was estimated to be 3 min (Fig. 2c). Using this parameter, we evaluated the accuracy for determination of the onset time by fitting a single exponential to the dataset quantifying the fluorescence increase obtained within an arbitrary time interval. The accuracy of computed onset time was determined within 0.1 min when using a dataset with 1-min time intervals (Fig. S4).

The increase in the amount of fluorescence signal depended upon the quantity of IL-1β injected (Fig. 2c). However, the absolute amount of secreted cytokine could not be determined because of the difficulties in controlling the local concentration of cytokines within an open-ended microwell to generate a standard curve. Additionally, immobilized cytokine captured by antibody on the MWA surface was considered to be part of the overall secreted cytokine, while the non-immobilized fraction diffused into the medium. The captured ratio would depend upon an uncontrollable variable, such as the height of the cytokine release point (which determines the probability of the cytokine encountering the capture antibody). Therefore, the assay platform developed in this study was best suited for detection of the onset of secretory molecule secretion from single cells at high time resolution (probably less than 1 min) while also providing semi-quantitative data on secreted molecules. In experiments performed using microwells closed with sealing oil, the platform could detect the signal from 2,000 molecules of IL-1β in a microwell (Supplementary Fig. S5).

Real-time monitoring of IL-6 secretion from single living monocytes within a 1-min time interval. As a proof-of-concept experiment, we assessed the performance of our assay platform for time-resolved observation using lipopolysaccharide (LPS)-stimulated human peripheral blood monocytes by simultaneous detection of cytokine secretion and live/dead signals. We confirmed that proinflammatory cytokines were detected in the culture supernatant of 1×10^5 monocytes stimulated with 1 μg/mL LPS (first priming; Supplementary Fig. S6). Among the detectable cytokines, we selected interleukin 6 (IL-6) as a typical cytokine, known to be released using classical pathways involving ER/Golgi trafficking[11].

First, we examined the reactivity and viability of monocytes in the MWA from snapshot measurements of 2,500 microwells after LPS stimulation for 4 h. Of the 584 cells observed from 2,500 microwells, 23 cells displayed the IL-6 signal (4%). Calcein (+)/SYTOX (−) living cells accounted for 60% of the total cells, but 91% of IL-6–positive cells. Next, 40 microwells were scanned for 4 h for real-time IL-6 secretion imaging at 1-min time intervals. After three independent experiments, we could analyse 71 single cells, including 56 living cells; 7 individual cells were observed to secrete IL-6 (representative images are displayed in Fig. 3a and Supplementary movie 1). IL-6 signals increased gradually for over 1 h after stimulation (Fig. 3b) without change in the SYTOX signal (Fig. 3b), as observed in the displayed dead cell (Fig. 3c). All the remaining IL-6–secreting cells continued to survive during the observation period. These results demonstrated that the single-cell secretion assay platform enabled us to monitor physiological secretion of IL-6 from live monocytes.

Simultaneous imaging of extracellular IL-1β secretion and plasma membrane integrity. The mechanism underlying IL-1β secretion remains poorly understood, although it is known that IL-1β is a key mediator of inflammation[12–14]. Several researchers have proposed various mechanisms for IL-1β secretion[15,16]; however, many details remain to be validated due to a lack of techniques for monitoring real-time secretion processes of IL-1β at single-cell resolution. Therefore, we monitored IL-1β secretion from individual monocytes at high temporal resolution in parallel with observation of the cellular physiological states at the time of secretion.

In this study, monocytes were costimulated with both LPS and adenosine triphosphate (ATP), because IL-1β release from monocytes is known to require a second signal (i.e. ATP) to activate the intracellular inflammasome in addition to priming with pathogen-associated molecular stimuli (i.e. LPS)[17–19]. Glycine was added to the culture medium during stimulation because glycine blocks cytolytic release of pro–IL-1β without affecting the secretion of mature IL-1β (Supplementary Fig. S6)[15,20,21].

Before real-time monitoring, we analysed IL-1β secretion and the live/dead state by snapshot secretion measurements of single cells with calcein/SYTOX staining (Fig. 4a) in 2,500 microwells at 4 h after LPS/ATP stimulation (Supplementary Fig. S7). This snapshot measurement demonstrated that approximately 30% of single monocytes secreted IL-1β. Interestingly, 99% of these IL-1β–secreting cells lost the calcein signal and were stained with SYTOX. When lower LPS concentration (10 ng/mL) was tested, both the number of IL-1β-secreting cells and the amount of secreted IL-1β per monocytes were decreased while the percentage of dead cells was only slightly affected (Supplementary Table S1). The concomitant disappearance of calcein and the increase in SYTOX signal reflect the compromised status of the cell membrane. Therefore, these results suggested some degree of association between IL-1β secretion and the loss of cell membrane integrity, exhibiting a sharp contrast with IL-6 secretion from LPS-stimulated monocytes (in which the vast majority of IL-6 secreting cells remained calcein-positive).

We then performed real-time secretion imaging of IL-1β from monocytes, focusing on whether IL-1β secretion was preceded or followed by a loss of cellular membrane integrity. The experiments

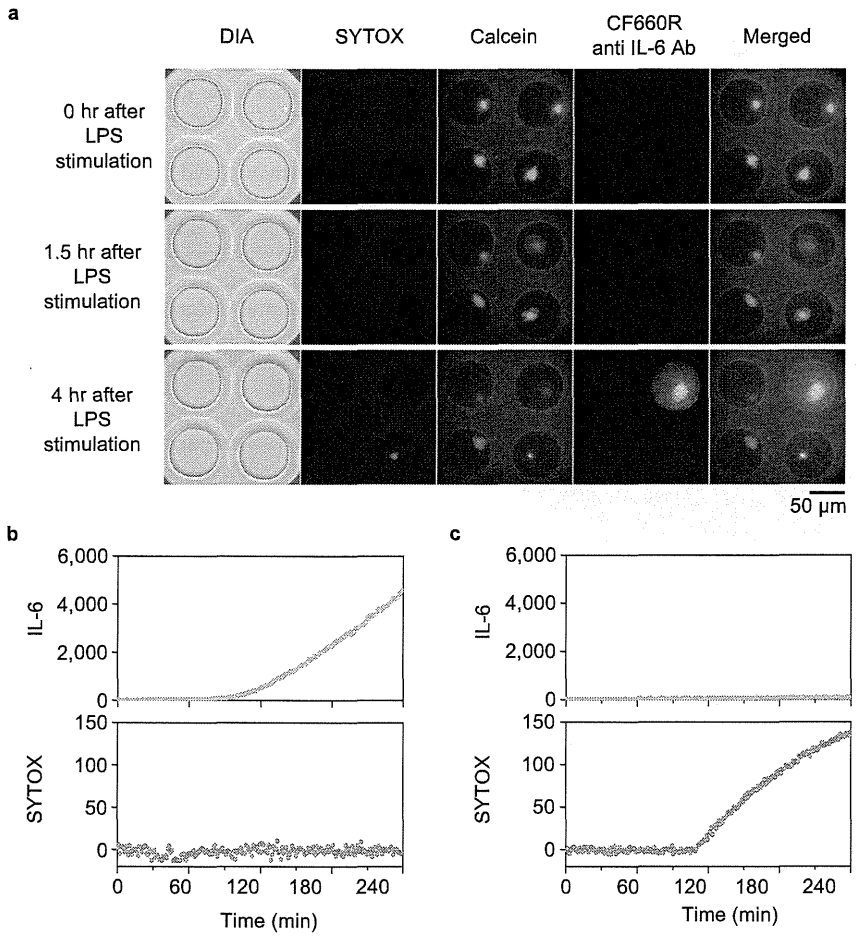

Figure 3 | Time-resolved monitoring of IL-6 secretion after a classical secretion pathway. Calcein-charged human peripheral blood monocytes were introduced into the MWA chip. Signals of SYTOX, calcein and IL-6 secretion were observed with 1-min time intervals after administration of 1 μg/mL of LPS. (a) Representative images of multichannel microscopy. Morphological features of a human monocyte were monitored under diascopic illumination (DIA). The fluorescence signal of SYTOX-stained nuclei was magenta (SYTOX), that of calcein-stained cell bodies was green (Calcein), and that of secreted IL-6 was yellow (CF660R anti IL-6 Ab). Merged images of these three fluorescence signals are also displayed (Merged). Each image was generated at the described time point. Scale bar, 50 μm. Although cells floated soon after LPS stimulation, cells began to adhere to the microwell bottom at 1.5 h after LPS stimulation, with some exhibiting the IL-6 signal at 4 h after LPS stimulation. Although the fluorescence intensity of calcein per pixel was apparently decreased due to the cell deformation, it was distinct from a sharp drop of calcein signal observed for dead cells like in the bottom-right well. The cells that underwent cell death showed elevation of the SYTOX signal. (b), (c) Time course of the average intensity of IL-6 and SYTOX signals within microwells shown in Figure 3a: the top right (b) or the bottom right (c) microwell. (b) The IL-6 secretion signal gradually increased from 80 min after LPS stimulation without any change in SYTOX signal. (c) Typical example of a dead cell. Only the SYTOX signal was increased.

were performed twice, measuring 54 individual monocytes, 20 of which secreted detectable quantities of IL-1β. While all of these cells were calcein-positive before ATP stimulation, they lost their calcein signal and subsequently stained with SYTOX, consistent with the aforementioned snapshot observations (Supplementary movie 2 and Fig. 4b). Disappearance of the calcein signal occurred rapidly and was completed within a few minutes. By contrast, the observed increases in SYTOX signalling consisted of two phases: the first occurred gradually upon ATP stimulation and the second occurred abruptly at various moments following ATP stimulation. These two phases suggest that cell membrane permeability for SYTOX influx was altered through multiple stages.

Surprisingly, IL-1β secretion appeared to coincide with calcein disappearance and the second SYTOX influx (Supplementary movie 2 and Fig. 4c). The increase in the signal of IL-1β secretion occurred as a concave-down function, suggesting IL-1β was secreted in a burst release pattern (Supplementary Fig. S8). To evaluate the association between these events, the transition times were determined by curve fitting of the equation (1), (2), or (3) to the mean fluorescence intensities over time and were compared with one another (Supplementary Fig. S9). Although the response times after ATP stimulation were quite heterogeneous among cells, the transition time of calcein disappearance, SYTOX influx, and IL-1β release were quite similar in most cells (Fig. 5a and b). By focusing on the timeline of these events, lag times between SYTOX influx or IL-1β release and calcein disappearance were calculated. The SYTOX influx and the calcein disappearance (both resulting from membrane imperfections) occurred simultaneously or nearly simultaneously, and SYTOX influx was only slightly delayed following calcein disappearance (mean, 0.2 min; Fig. 5c). By contrast, IL-1β release occurred several minutes following calcein disappearance (mean, 2.0 min, except for 2 outliers; Fig. 5d), and its lag times were more variable than those of SYTOX influx. Two outliers exhibited extremely long delays (44.5 and 105.9 min) in IL-1β release after calcein disappearance. These results indicated that burst release of IL-1β was preceded by loss of cell membrane integrity.

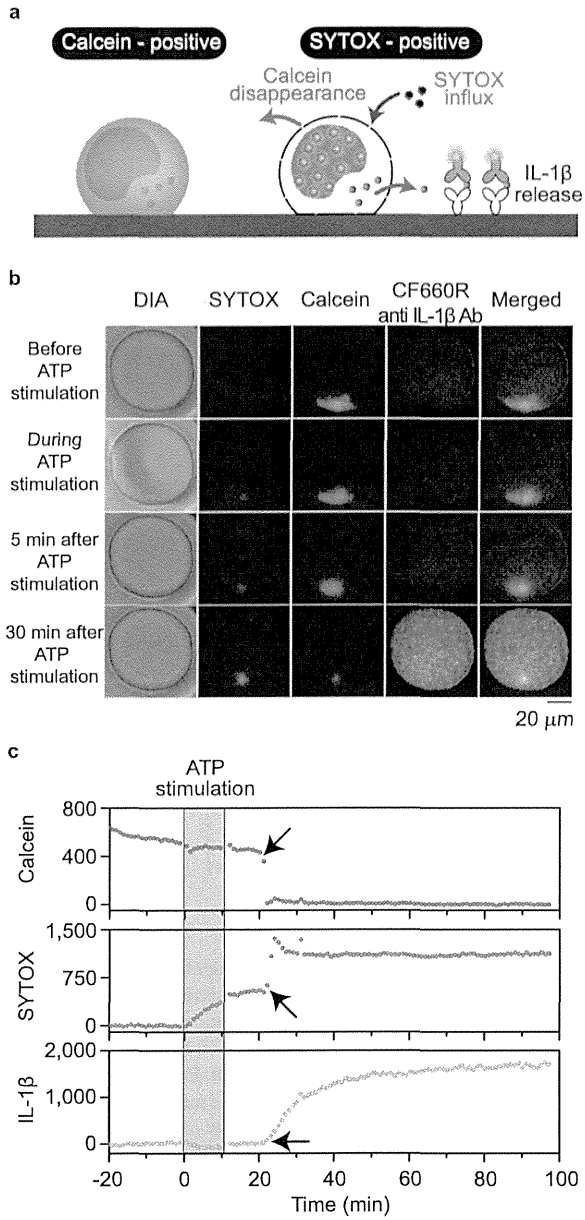

Figure 4 | Time-resolved monitoring of IL-1β secretion on the PDMS MWA chip. (a) Schematic of simultaneous monitoring of IL-1β secretion and cell membrane integrity using calcein and SYTOX staining. SYTOX influx and fluorescent calcein disappearance was observed due to compromised plasma membrane integrity. (b) Representative images of multichannel microscopy. Morphological features of a human monocyte were monitored under diascopic illumination (DIA). The fluorescence signal of SYTOX-stained nuclei was magenta (SYTOX), that of a calcein-stained cell bodies was green (Calcein), and that of secreted IL-1β was yellow (CF660R anti IL-1β Ab). Merged images of these three fluorescence signals are also displayed (Merged). Each image was obtained at the described period. Scale bar, 20 μm. (c) Example of the signal time course during time-resolved monitoring. Grey bands represent the period when the monocytes were exposed to ATP. Arrows represent the transition time of the respective signals.

Discussion

In this study, we have developed a novel assay platform for real-time imaging of secretion at the single cell level at 1-min intervals. The dynamics of cytokine secretion against external stimuli have conventionally been investigated using a bulk population of cells with the same phenotype, based on the premise that these cells always display uniform responses. However, contrary to this premise, we have observed a wide distribution of onset time for IL-1β release triggered by ATP stimulation from individual human peripheral blood monocytes. Temporal heterogeneities at the single cell level have been demonstrated by many studies, but have been limited to intracellular processes, e.g. intracellular calcium elevation[22]. Our results indicated that extracellular reactions, such as protein secretion, were also chronologically heterogeneous at the single cell level. Furthermore, we successfully performed simultaneous measurement of cell membrane integrity and IL-1β release, indicating that our platform allowed for elucidation of the chronological relationship between intracellular process and the extracellular reaction at the single-cell level.

Imaging methods for secretion dynamics have been poorly developed for two primary reasons: First, secreted molecules disperse too rapidly in solution for efficient onsite monitoring. Second, a molecule of interest must be tagged by sensing moieties, but the tagging processes for molecular visualization are often accompanied with greater risks of generating artifacts, including functional modifications. Indeed, this latter point is the most serious limitation of live-cell imaging in general. The platform developed in this study permitted us to bypass such issues by immobilizing and labelling target molecules in the extracellular space. The detection strategy offers an advantage in its non-invasive monitoring of the physiological response of living cells, including clinical samples. A similar methodology with a label-free technique based upon nanoplasmonic imaging has been developed, although it is only applicable to up to three cells per experiment[23]. Sandwich FIA-based assay is expected to be a more sensitive and specific approach for small molecules like cytokines than the plasmonic approach, since the plasmonic signal is proportional to the molecular weight of the binding molecule.

Our platform uses MWAs that effectively trap floating cells as well as secreted cytokine molecules. This compartmentalization permitted integration of independently isolated single cells within a small area to increase the number of observable cells. More specifically, observation of a large number of cells made it feasible to perform statistical analyses on a small population of secreting monocytes. The open architecture of this device is well suited for cell manipulation using conventional tools, allowing for complex experimental arrangements. Additionally, the open architecture was beneficial for the maintenance of cellular physiology, because prolonged isolation within closed microwells may influence cellular conditions, e.g. oxygen starvation[24]. In this work, MWA chips were fabricated with PDMS, suitable for live cell imaging because of its biocompatibility[25]. PDMS offers low cost and fast processing in fabrication of the MWA chip. The only inconvenience was its higher refractive index than that of water, requiring a higher critical angle of the incident light for TIRFM. We resolved the issue by using an objective lens of high numerical aperture to achieve incidence angles greater than the critical angle for a glass/PDMS interface.

In our experiments, the rate of the apparent increase in the TIRF signal was 15 times slower than that of the apparent capture rate of the antigen onto the bottom surface of the MWA chip. This phenomenon was observed probably because (1) the difference in the local concentration of antibodies near the bottom surface and (2) decrease of the unbound antigen by diffusion followed pseudo first-order kinetics with a time constant of approximately 0.9 min (Supplementary Fig. S2). The increase in the concentration of fluorescent detection antibody accelerates the rate of the apparent increase in the TIRF signal while decreasing the detection sensitivity because of elevated background.

The 2,000-molecule detection limit for IL-1β is as low as that reported earlier[6,8]. The average rate of IL-1β secretion from a single monocyte calculated from bulk measurements (Supplementary

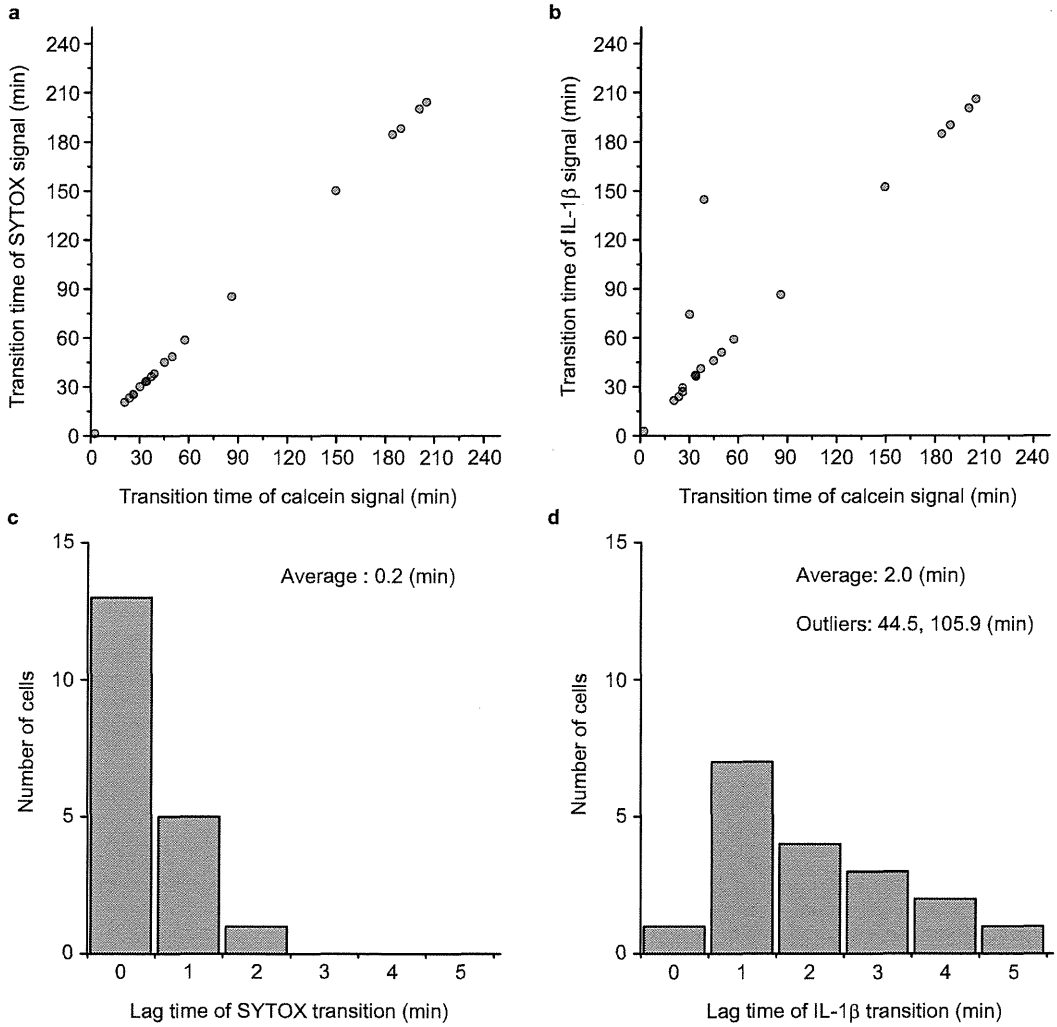

Figure 5 | High concordance of the three transition times observed in individual single cells. (a), (b) Scatter plots of the signal transition times for SYTOX or IL-1β versus calcein. Signal transition occurred virtually simultaneously between calcein, SYTOX, and IL-1β. Each circle represents 20 individual monocytes. (d) Histograms of the lag times of SYTOX or IL-1β signal transition after the calcein disappearance. The lag times of SYTOX were distributed in a narrow range near 0, whereas those of IL-1β showed a wider distribution.

Fig. S6) was approximately 40 molecules/min if all the monocytes continuously secreted IL-1β, implying that it takes more than 50 min to detect IL-1β secretion using our assay system. However, we observed sharp rise of IL-1β signals in some cells, which indicated the massive IL-1β secretion was in a transiently-released manner. This shows the power of our real-time imaging system, which allows the dynamic analysis with improved time resolution as well as analysis for temporal cell-to-cell variations in protein secretion. The concave-down increase of the IL-1β secretion signal also suggested a burst release, rather than continuous secretion of IL-1β. Use of the time constant for association of detection antibody, obtained from the results of a model experiment, enabled estimation of the onset time of a massive burst release of IL-1β with a time resolution of <1 min. The accuracy of onset time estimation was sufficient for identifying the relationship of biophysical phenomena on a minute-based time scale. Smaller time intervals of data acquisition improve the accuracy of curve fitting within a predetermined time window of 5 min, but simultaneously reduce the number of observable microwells during a single cycle of scanning. The nonequilibrium characteristics of the antigen-antibody interaction in the open structure made it difficult to establish a series of concentration standards, but were considered an acceptable trade-off for long-term monitoring of cellular activities.

In addition to previous studies[15,16], our snapshot measurement of IL-1β secretion from monocytes stained with live/dead indicators demonstrated that most of the IL-1β–secreting cells were dead. These observations allow for several interpretations, because the chronological relationship between IL-1β release and the change in calcein/SYTOX staining remained unknown. However, our real-time monitoring experiment showed that IL-1β release always occurred after calcein/SYTOX transition. Since the monitored cells were prepared in the presence of glycine[16], both the calcein/SYTOX transition and IL-1β release were likely caused by pore formation on the plasma membrane, and not by cytolysis[16,17]. Two phases of SYTOX influx were observed during and after ATP administration to monocytes, suggesting multiple cell-permeable processes, such as the ATP-dependent opening of a P2X7 pore allowing for the passage of molecules of up to 900 Da in size[19,26] and large pore formation mediated by caspase 1[20]. Moreover, our analysis of high temporal resolution uncovered a several-minute lag between calcein/SYTOX transition and IL-1β release. This lag time suggested that the calcein/SYTOX-permeable

cells require another process to release IL-1β, a process that remains to be elucidated.

The cytokine secretion dynamics in monocytes described herein implies that cell-cell communication via cytokines also varies widely with regard to timing. Further studies are required to clarify the manner in which heterogeneous cell-cell communication affects the maintenance of homeostasis of the immune system under various complex physiological situations, such as T-helper subset differentiation[27] and the switch from acute resolving to chronic persistent inflammation[28]. The establishment of the real-time secretion assay platform described in this study opens the way to addressing these issues through the monitoring of cytokine secretion dynamics in parallel with intracellular events at single-cell resolution.

Methods

Reagents. The DuoSet ELISA Development System was purchased from R&D Systems (Minneapolis, MN, USA), and the set of capture and detection antibodies was used for sandwich immunoassays for human IL-1β (DY201). Human IL-6 monoclonal antibody (clone 6708; MAB206) and human IL-6 biotinylated affinity-purified polyclonal antibody (BAF206) were also purchased from R&D Systems. Adenosine 5′-triphosphate disodium salt hydrate (ATP, A7699) and lipopolysaccharides from *Escherichia coli* 055:B5 (LPS, L4524) were purchased from Sigma-Aldrich (St. Louis, MO, USA). Lipidure BL802, a water-soluble polymer of 2-methacryloyloxy ethyl phosphorylcholine, was purchased from NOF Corporation (Tokyo, Japan). Calcein AM (C3099) and SYTOX Blue nucleic acid stain (S11348) were purchased from Life Technologies (Carlsbad, CA, USA). CF660R streptavidin was purchased from Biotium (29040; Hayward, CA, USA). Dimethyl pimelimidate-2HCl (DMP, 21666) was purchased from Thermo Fisher Scientific (Rockford, IL, USA). Foetal bovine serum (FBS, s1560) was purchased from Biowest (Nuaillé, France).

Cell culture. The incubation of cells was performed in a CO_2 incubator at 37°C in a humidified atmosphere with 5% CO_2, unless otherwise indicated. For the isolation of human peripheral blood monocytes, 20 mL of venous blood was drawn from a healthy donor after obtaining institutional approval of the ethical committee of the Kyoto University Hospital, in accordance with Declaration of Helsinki. Monocytes from different donors were used for different experiments. The cell fraction was separated with Lymphoprep (Axis-Shield, Dundee, UK) according to the manufacturer's instructions. $CD14^+$ monocytes were sequentially purified by MACS (Miltenyi Biotec, Bergisch Gladbach, Germany) with a negative selection reagent (i.e. monocyte isolation kit II) and a positive selection reagent (i.e. CD14 microbeads). The isolated monocytes were incubated overnight in RPMI medium containing 10% FBS.

Optical arrangement. All measurements were performed with a completely automated inverted microscope (ECLIPSE Ti-E; Nikon, Tokyo, Japan) equipped with a high NA 60× objective lens (TIRF 60 × H; NA, 1.49; Nikon). The microscope was customized to introduce external laser beams (635 nm; Radius 635-25; Coherent, Santa Clara, CA, USA) at the indicated incident angle to actualize TIRF illumination. The following sets of excitation (Ex) and emission (Em) filters and a dichroic mirror (DM) were used with a high-pressure xenon lamp: for SYTOX, Ex = FF01-448/20-25, Em = FF01-482/25-25, and DM = Di02-R442-25x36; and for calcein, Ex = FF02-472/30-25, Em = FF01-520/35-25, and DM = FF495-Di03-25x36. The following Ex and Em filters and DM were used with the 632 nm laser for the CF660R dye: Ex = FF02-628/40-25, Em = FF01-692/40-25, and DM = FF660-Di02-25x36. These optical filters were purchased from Semrock (Rochester, NY, USA). Each image was projected on an EM-CCD camera (ImagEM C9100-13; Hamamatsu Photonics K.K., Sizuoka, Japan) through a 0.7× lens (C-0.7x DXM Relay Lens; Nikon). A stage-top incubator (ONICS; Tokai Hit Co., Shizuoka, Japan) was used to control temperature, humidity, and gas concentration.

MWA chips. MWA chips were prepared from PDMS and microscopic-grade coverslips. The PDMS MWA chip was prepared as follows: A thin PDMS sheet, consisting of a 50 × 50 array of 50-μm or 70-μm through-holes with 100-μm centre-to-centre spacing and 80-μm thickness, was purchased from Fluidware Technologies (Saitama, Japan). The PDMS sheet and a glass slide were permanently bonded together after the contact surfaces between them were plasma-treated (SEDE-PFA; Meiwafosis, Tokyo, Japan). The bare glass surfaces that now functioned as the bottom of the microwells after bonding were aminated with Vecatabond Reagent (SP-1800; Vector Laboratories, Burlingame, CA, USA). The chip was mounted on a coverslip holder (Attofluor cell chamber, A7819; Life Technologies) adjacent to another PDMS block (Sylgard184; Dow Corning Toray, Tokyo, Japan) with an 8-mm diameter through-hole that served as a reservoir well. The interstices between the PDMS-glass chip and the PDMS block were filled with uncured PDMS. The integrated chip was baked at 130°C for 3 h.

A 100-μL mixture of capture antibodies (100 μg/mL) and dimethyl pimelimidate-2HCl (DMP; 7 mg/mL) was loaded onto the aminated glass surface to fix the capture antibody. The surface was blocked with monoethanolamine (0.1 M, pH 8.2) and Lipidure reagent (0.2% [w/v]), and stored at 4°C until use.

Preparation of detection medium. Detection antibody labelled with biotin was coupled with CF-labelled streptavidin at 1 : 10 molar ratios at room temperature in the dark for 3 h. Unoccupied sites on streptavidin were blocked with excess dPEG4-biotin acid (10199; Quanta BioDesign, Ltd., Powell, OH, USA). Unconjugated streptavidin and dPEG4-biotin were removed by ultrafiltration (Amicon Ultra-0.5, 100 kDa; Merck Millipore, Billerica, MA, USA). The detection media contained prepared CF-labelled detection antibody (30 nM), BSA (2.5% [w/v]), and the indicated combination of the following additives (with the final concentrations): SYTOX (0.8 μM), glycine (5 mM), LPS (1 μg/mL), and/or ATP (5 mM).

Handling and treatment of cells. Monocytes were stimulated with LPS for 3 h and incubated with 0.4 μM Calcein AM for 15 min before IL-1β secretion analysis on a PDMS MWA chip. The cells were washed with fresh medium and recovered from the bottom of 96-well plates by gentle pipetting. Approximately 2,000 cells were introduced into an MWA chip and allowed to settle by gravity for 10 min in a CO_2 incubator. Next, the medium was replaced with the detection medium containing SYTOX, glycine, and LPS. The cells were first monitored for 20 min before ATP stimulation; after ATP administration, monitoring was resumed during the 10-min incubation period. The medium was then replaced with fresh detection medium containing SYTOX, glycine, and LPS. Measurements were then resumed and continued for 4 h.

Time-resolved monitoring of cytokine secretion from stimulated monocytes. Ten positions were selected in order to include as many single cell-containing microwells as possible. Monocytes in the selected position of microwells were monitored at 1-min intervals by multichannel microscopy, i.e. DIA images, epifluorescence images for calcein and SYTOX, and TIRF images for CF660R for cytokine secretion at controlled temperature and gas concentrations. The MFIs of each microwell at each time point were measured with the NIS Elements imaging software.

Transition time estimation of calcein, SYTOX and IL-1β signals obtained from LPS/ATP stimulated monocytes. The transition time of calcein disappearance, SYTOX influx, and IL-1β release were detected by data analysis software (Origin 8.6; OriginLab Co., Northampton, MA, USA) by using the following equations:

$$I_c(t) = \begin{cases} I_{c0} + I_{c1} + m_c t & , \ t < t_{c0} \\ I_{c0} + (I_{c1} + m_c t_{c0}) \exp\{-(t - t_{c0})/\tau_c\}, & t \geq t_{c0} \end{cases} \quad (1)$$

for calcein disappearance,

$$I_s(t) = \begin{cases} I_{s0} + m_s t & , \ t < t_{s0} \\ I_{s0} + m_s t + I_{s1}[1 - \exp\{-(t - t_{s0})/\tau_s\}], & t \geq t_{s0} \end{cases} \quad (2)$$

for SYTOX influx, and

$$I_i(t) = \begin{cases} I_{i0} + m_i t & , \ t < t_{i0} \\ I_{i0} + m_i t + I_{i1}[1 - \exp\{-(t - t_{i0})/\tau_i\}], & t \geq t_{i0} \end{cases} \quad (3)$$

for IL-1β release, where $I(t)$ represents intensity, I_0 represents the background, m represents intensity drift, I_1 represents amplitude, t_0 represents transition time, and τ represents the time constant of exponential decay for each fluorescence signal. The subscripts c, s, and i of each parameter indicate calcein, SYTOX, and IL-1β labelling, respectively. The time constant of IL-1β (τ_i) was determined from a supplementary experiment with recombinant IL-1β (Fig. 2). The IL-1β secretion dataset was fitted by equation (3).

1. Gnecchi, M., Zhang, Z. P., Ni, A. G. & Dzau, V. J. Paracrine Mechanisms in Adult Stem Cell Signaling and Therapy. *Circ Res* **103**, 1204–1219 (2008).
2. Lander, A. D. How Cells Know Where They Are. *Science* **339**, 923–927 (2013).
3. Stastna, M. & Van Eyk, J. E. Secreted proteins as a fundamental source for biomarker discovery. *Proteomics* **12**, 722–735 (2012).
4. Rothenberg, E. V. Cell lineage regulators in B and T cell development. *Nat Immunol* **8**, 441–444 (2007).
5. Lacy, P. & Stow, J. L. Cytokine release from innate immune cells: association with diverse membrane trafficking pathways. *Blood* **118**, 9–18 (2011).
6. Ma, C. *et al.* A clinical microchip for evaluation of single immune cells reveals high functional heterogeneity in phenotypically similar T cells. *Nat Med* **17**, 738–743 (2011).
7. Love, J. C., Ronan, J. L., Grotenbreg, G. M., van der Veen, A. G. & Ploegh, H. L. A microengraving method for rapid selection of single cells producing antigen-specific antibodies. *Nat Biotechnol* **24**, 703–707 (2006).
8. Han, Q., Bagheri, N., Bradshaw, E. M., Hafler, D. A., Lauffenburger, D. A. & Love, J. C. Polyfunctional responses by human T cells result from sequential release of cytokines. *P Natl Acad Sci USA* **109**, 1607–1612 (2012).
9. Sasuga, Y. *et al.* Single-cell chemical lysis method for analyses of intracellular molecules using an array of picoliter-scale microwells. *Anal Chem* **80**, 9141–9149 (2008).
10. Salehi-Reyhani, A. *et al.* A first step towards practical single cell proteomics: a microfluidic antibody capture chip with TIRF detection. *Lab Chip* **11**, 1256–1261 (2011).
11. Stanley, A. C. & Lacy, P. Pathways for Cytokine Secretion. *Physiology* **25**, 218–229 (2010).

12. Dinarello, C. A. Biologic basis for interleukin-1 in disease. *Blood* **87**, 2095–2147 (1996).
13. Fujisawa, A. *et al.* Disease-associated mutations in CIAS1 induce cathepsin B-dependent rapid cell death of human THP-1 monocytic cells. *Blood* **109**, 2903–2911 (2007).
14. Tanaka, T. *et al.* Induced pluripotent stem cells from CINCA syndrome patients as a model for dissecting somatic mosaicism and drug discovery. *Blood* **120**, 1299–1308 (2012).
15. Bergsbaken, T., Fink, S. L. & Cookson, B. T. Pyroptosis: host cell death and inflammation. *Nat Rev Microbiol* **7**, 99–109 (2009).
16. Eder, C. Mechanisms of interleukin-1beta release. *Immunobiology* **214**, 543–553 (2009).
17. Lopez-Castejon, G. & Brough, D. Understanding the mechanism of IL-1beta secretion. *Cytokine Growth Factor Rev* **22**, 189–195 (2011).
18. Mariathasan, S. *et al.* Cryopyrin activates the inflammasome in response to toxins and ATP. *Nature* **440**, 228–232 (2006).
19. Ward, J. R. *et al.* Temporal Interleukin-1 beta Secretion from Primary Human Peripheral Blood Monocytes by P2X7-independent and P2X7-dependent Mechanisms. *Journal of Biological Chemistry* **285**, 23145–23156 (2010).
20. Fink, S. L. & Cookson, B. T. Caspase-1-dependent pore formation during pyroptosis leads to osmotic lysis of infected host macrophages. *Cell Microbiol* **8**, 1812–1825 (2006).
21. Verhoef, P. A., Kertesy, S. B., Estacion, M., Schilling, W. P. & Dubyak, G. R. Maitotoxin induces biphasic interleukin-1beta secretion and membrane blebbing in murine macrophages. *Mol Pharmacol* **66**, 909–920 (2004).
22. Roy, S. S. & Hajnoczly, G. Calcium, mitochondria and apoptosis studied by fluorescence measurements. *Methods* **46**, 213–223 (2008).
23. Raphael, M. P., Christodoulides, J. A., Delehanty, J. B., Long, J. P. & Byers, J. M. Quantitative Imaging of Protein Secretions from Single Cells in Real Time. *Biophys J* **105**, 602–608 (2013).
24. Molter, T. W. *et al.* A New Approach for Measuring Single-Cell Oxygen Consumption Rates. *IEEE Trans Autom Sci Eng* **5**, 32–42 (2008).
25. Belanger, M. C. & Marois, Y. Hemocompatibility, biocompatibility, inflammatory and in vivo studies of primary reference materials low-density polyethylene and polydimethylsiloxane: A review. *J Biomed Mater Res* **58**, 467–477 (2001).
26. Ferrari, D. *et al.* The P2X(7) receptor: A key player in IL-1 processing and release. *Journal of Immunology* **176**, 3877–3883 (2006).
27. Zhu, J. F. & Paul, W. E. Heterogeneity and plasticity of T helper cells. *Cell Res* **20**, 4–12 (2010).
28. Nathan, C. & Ding, A. H. Nonresolving Inflammation. *Cell* **140**, 871–882 (2010).

Acknowledgments

We thank Katsuyuki Shiroguchi (RIKEN) and Hirotsugu Oda (Kyoto Univ.) for critical reading of the manuscript. This work was partly supported by the Special Postdoctoral Researchers Program of RIKEN, by a Grant-in-Aid for Young Scientists (B) (no. 23770189, to Y.S.), a Grant-in-Aid for Scientific Basic Research (C) (no. 25440074, to Y.S.) and for Scientific Basic Research (S) (no. 23226010, to S.S.) from MEXT, Japan.

Author contributions

Y.S., Y.H. and O.O. conceived the methods described; Y.S. and M.Y. set up the optical instruments; A.N., J.M. and S.S. contributed to the technical development of the MWA chip; Y.S. and N.S. prepared MWA chips; K.I., R.N. and T.H. performed and supervised clinical sample preparation; and Y.S. performed imaging experiments and analysis. The manuscript was prepared by Y.S., M.Y., and O.O. after discussion with all the authors.

Additional information

Supplementary information accompanies this paper at http://www.nature.com/scientificreports

Competing financial interests: The authors declare no competing financial interests.

How to cite this article: Shirasaki, Y. *et al.* Real-time single-cell imaging of protein secretion. *Sci. Rep.* **4**, 4736; DOI:10.1038/srep04736 (2014).

Aicardi-Goutières Syndrome Is Caused by *IFIH1* Mutations

Hirotsugu Oda,[1,2] Kenji Nakagawa,[1] Junya Abe,[1,3] Tomonari Awaya,[1] Masahide Funabiki,[4] Atsushi Hijikata,[5] Ryuta Nishikomori,[1,*] Makoto Funatsuka,[6] Yusei Ohshima,[7] Yuji Sugawara,[8] Takahiro Yasumi,[1] Hiroki Kato,[4,9] Tsuyoshi Shirai,[5] Osamu Ohara,[2,10] Takashi Fujita,[4] and Toshio Heike[1]

Aicardi-Goutières syndrome (AGS) is a rare, genetically determined early-onset progressive encephalopathy. To date, mutations in six genes have been identified as etiologic for AGS. Our Japanese nationwide AGS survey identified six AGS-affected individuals without a molecular diagnosis; we performed whole-exome sequencing on three of these individuals. After removal of the common polymorphisms found in SNP databases, we were able to identify *IFIH1* heterozygous missense mutations in all three. In vitro functional analysis revealed that *IFIH1* mutations increased type I interferon production, and the transcription of interferon-stimulated genes were elevated. *IFIH1* encodes MDA5, and mutant MDA5 lacked ligand-specific responsiveness, similarly to the dominant *Ifih1* mutation responsible for the SLE mouse model that results in type I interferon overproduction. This study suggests that the *IFIH1* mutations are responsible for the AGS phenotype due to an excessive production of type I interferon.

Aicardi-Goutières syndrome (AGS [MIM 225750]) is a rare, genetically determined early-onset progressive encephalopathy.[1] Individuals affected with AGS typically suffer from progressive microcephaly associated with severe neurological symptoms, such as hypotonia, dystonia, seizures, spastic quadriplegia, and severe developmental delay.[2] On brain imaging, AGS is characterized by basal ganglia calcification, white matter abnormalities, and cerebral atrophy.[3,4] Cerebrospinal fluid (CSF) analyses show chronic lymphocytosis and elevated levels of IFN-α and neopterin.[3–5] AGS-affected individuals are often misdiagnosed as having intrauterine infections, such as TORCH syndrome, because of the similarities of these disorders, particularly the intracranial calcifications.[1] In AGS, etiological mutations have been reported in the following six genes: *TREX1* (MIM 606609), which encodes a DNA exonuclease; *RNASEH2A* (MIM 606034), *RNASEH2B* (MIM 610326), and *RNASEH2C* (MIM 610330), which together comprise the RNase H2 endonuclease complex; *SAMHD1* (MIM 606754), which encodes a deoxynucleotide triphosphohydrolase; and *ADAR1* (MIM 146920), which encodes an adenosine deaminase.[6–9] Although more than 90% of AGS-affected individuals harbor etiological mutations in one of these six genes, some AGS-affected individuals presenting with the clinical characteristics of AGS still lack a genetic diagnosis, suggesting the existence of additional AGS-associated genes.[1]

We recently conducted a nationwide survey of AGS in Japan and reported 14 AGS-affected individuals.[10] We have since recruited three other Japanese AGS-affected individuals, and among these 17 individuals, we have identified 11 individuals with etiologic mutations; namely, *TREX1* mutations in six, *SAMHD1* mutations in three, and *RNASEH2A* and *RNASEH2B* mutations in one each. Of the remaining six individuals without a molecular diagnosis, trio-based whole-exome sequencing was performed in three whose parents also agreed to participate in further genome-wide analyses (Figure 1A). Genomic DNA from each individual and the parents was enriched for protein-coding sequences, followed by massively parallel sequencing. The extracted nonsynonymous or splice-site variants were filtered to remove those with minor allele frequencies (MAF) > 0.01 in dbSNP137. To detect de novo variants, any variants observed in family members, listed in Human Genetic Variation Database (HGVD), or with MAF > 0.02 in our in-house exome database were removed. To detect autosomal-recessive (AR), compound heterozygous (CH), or X-linked (XL) variants, those with MAF > 0.05 in our in-house database were removed (Figure S1 available online). All samples were collected with the written informed consents by parents, and the study protocol was approved by the ethical committee of Kyoto University Hospital in accordance with the Declaration of Helsinki.

After common polymorphisms were removed, we identified a total of 40, 18, 89, and 22 candidate variants under the de novo, AR, CH, and XL inheritance models, respectively, that were present in at least one of the three individuals (Table S1). Among them, missense mutations were identified in *IFIH1* (MIM 606951, RefSeq accession

[1]Department of Pediatrics, Kyoto University Graduate School of Medicine, Kyoto 6068507, Japan; [2]Laboratory for Integrative Genomics, RIKEN Center for Integrative Medical Sciences, Yokohama 2300045, Japan; [3]Department of Pediatrics, Kitano Hospital, Tazuke Kofukai Medical Research Institute, Osaka 5308480, Japan; [4]Laboratory of Molecular Genetics, Institute for Virus Research, Kyoto University, Kyoto 6068507, Japan; [5]Department of Bioscience, Nagahama Institute of Bio-Science and Technology, Nagahama 5260829, Japan; [6]Department of Pediatrics, Tokyo Women's Medical University, Tokyo 1628666, Japan; [7]Department of Pediatrics, Faculty of Medical Sciences, University of Fukui, Fukui 9108507, Japan; [8]Department of Pediatrics and Developmental Biology, Graduate School of Medical and Dental Sciences, Tokyo Medical and Dental University, Tokyo 1138510, Japan; [9]Precursory Research for Embryonic Science and Technology (PRESTO), Science and Technology Agency (JST), Kawaguchi 3320012, Japan; [10]Department of Human Genome Research, Kazusa DNA Research Institute, Kisarazu 2920818, Japan
*Correspondence: rnishiko@kuhp.kyoto-u.ac.jp
http://dx.doi.org/10.1016/j.ajhg.2014.06.007.

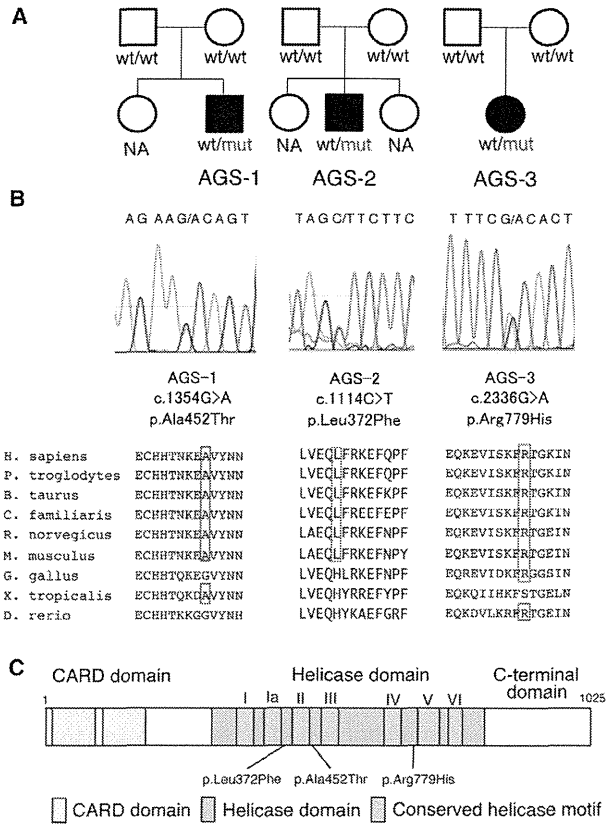

Figure 1. Pedigree Information for the AGS-Affected Individuals and Details of the *IFIH1* Mutations Identified

(A) The pedigrees of the three families indicating the AGS probands.

(B) Sanger sequencing chromatograms of the three *IFIH1* mutations found in the AGS-affected individuals. The locations of these mutations in the amino acid sequence of the MDA5 protein are shown in alignment with the conserved amino acid sequences from several species. This alignment was obtained via ClustalW2. The amino acids that are conserved with human are circled in red.

(C) The MDA5 protein domain structure with the amino acid substitutions observed in these AGS-affected individuals.

number NM_022168.2), which encodes MDA5 (RefSeq NP_071451.2). These missense mutations are c.1354G>A (p.Ala452Thr) in AGS-1; c.1114C>T (p.Leu372Phe) in AGS-2; and c.2336G>A (p.Arg779His) in AGS-3 (Figure 1B). None of the mutations are found in HGVD, including the 1,208 Japanese samples, or our in-house exome database of 312 Japanese individuals. Multiple-sequence alignment by ClustalW2 revealed that each of the amino acids affected by these mutations are conserved among mammals (Figure 1B). The subsequent amino acid alterations were all suggested to be disease causing in at least one of the four function-prediction programs used (Table 1). None of the other genes identified in the de novo inheritance model, or any of the genes identified in the other three inheritance models, were mutated in all three individuals. The *IFIH1* mutations identified were validated by Sanger sequencing. The other coding exons of *IFIH1* were also examined by Sanger sequencing, and no other mutations were found.

MDA5 is one of the cytosolic pattern recognition receptors that recognizes double-stranded RNA (dsRNA).[11] MDA5 consists of N-terminal tandem CARD domains, a central helicase domain, and a C-terminal domain (Figure 1C). When bound to dsRNA, MDA5 forms a closed, C-shaped ring structure around the dsRNA stem and excludes the tandem CARD as well as creates filamentous oligomer on dsRNA.[12] It is hypothesized that the tandem CARD interacts each other and activates MAVS on the mitochondrial outer membrane. Oligomerization of MAVS induces TBK1 activation, IRF3 phosphorylation, and induction of type I interferon transcription, resulting in the activation of a large number of interferon-stimulated genes (ISGs).

The neurological findings of the individuals with these *IFIH1* mutations are typical of AGS (Table S2). They were born with appropriate weights for their gestational ages without any signs of intrauterine infection. However, they all demonstrated severe developmental delay in early infancy associated with progressive microcephaly. No arthropathy, hearing loss, or ophthalmological problems were observed. As for extraneural features, all three individuals had at least one of the following autoimmune features: positivity for autoantibodies, hyperimmunoglobulinemia, hypocomplementemia, and thrombocytopenia. Notably, none of the individuals with *IFIH1* mutations had chilblain lesions, although all the five individuals with *TREX1* mutations and two of the three individuals with *SAMHD1* mutations in the Japanese AGS cohort showed chilblain lesions.[10] Individuals with *SAMHD1* mutations and *IFIH1* mutations both show autoimmune features; however, chilblain lesions have been observed only in individuals with *SAMHD1* mutations.[10]

To predict the effects of the identified amino acid substitutions on MDA5, three-dimensional model structures of MDA5 mutants were generated from the crystal structure of human MDA5-dsRNA complex[12] (Protein Data Bank [PDB] code 4gl2), using PyMOL (Schroedinger) and MOE (Chemical Computing Group) (Figure S2A). The oligomeric model of MDA5 was generated using the electron microscopy imaging data of MDA5 filament lacking CARD domain[13] (Electron Microscopic Data Bank [EMDB] code 5444) (Figure S2B). The three amino acid substitutions in the AGS-affected individuals are all located within the helicase domain (Figures 1C and S2A). Because Ala452 directly contacts the dsRNA ribose O2′ atom, the p.Ala452Thr substitution probably affects the binding affinity to dsRNA due to an atomic repulsion between the side chain of Thr452 and the dsRNA O2′ atom (Figures S2C and S2D). Leu372 is located adjacent to the ATP binding pocket, and the p.Leu372Phe substitution could increase the side chain volume of the binding pocket, affecting its ATP hydrolysis activity (Figures S2E and S2F). In our oligomeric model, Arg779 is located at the interface between the two monomers, which is consistent with the

Table 1. Functional Predictions of the *IFIH1* Variants

Individuals	Nucleotide Change	Amino Acid Change	SIFT	PolyPhen2	Mutation Taster	PROVEAN
AGS-1	c.1354G>A	p.Ala452Thr	tolerated	benign	disease causing	neutral
AGS-2	c.1114C>T	p.Leu372Phe	tolerated	probably damaging	disease causing	neutral
AGS-3	c.2336G>A	p.Arg779His	tolerated	probably damaging	disease causing	deleterious

The potential functional effects of the *IFIH1* variants identified in the AGS-affected individuals were predicted via SIFT, PolyPhen2, Mutation Taster, and PROVEAN.

recent report showing that Lys777, close to Arg779, is in close proximity to the adjacent monomer.[12] Furthermore, in our model, Arg779 is in close to Asp572 on the surface of the adjacent monomer. We speculate that losing the positive charge due to the p.Arg779His substitution would possibly affect the electrostatic interaction between the MDA5 monomers (Figures S2G and S2H).

To connect the identified *IFIH1* mutations with the AGS phenotype, we examined the type I interferon signature in the individuals by performing quantitative RT-PCR (qRT-PCR) of seven ISGs.[14] Peripheral blood mononuclear cells (PBMCs) from the three AGS-affected individuals showed upregulation of ISG transcription (Figure 2), confirming the type I interferon signature in the individuals with *IFIH1* mutations.

To elucidate the disease-causing capability of the identified *IFIH1* mutations, three FLAG-tagged *IFIH1* mutant plasmids containing these mutations were constructed via site-directed mutagenesis. These plasmids were transiently expressed on human hepatoma cell line Huh7 and the *IFNB1* promoter activity as well as endogenous expression of *IFIT1* (MIM 147690) was measured 48 hr after transfection.[15] The three mutant plasmids activated the *IFNB1* promoter in Huh7 cells more strongly than the wild MDA5 and nearby missense variants reported in dbSNP (Figures 3 and S3). The upregulation of endogenous *IFIT1* was also observed in the transfected cells (Figure S4), suggesting that these AGS mutations enhance the intrinsic activation function of MDA5. Recent genome-wide association studies (GWASs) showed association of the *IFIH1* with various autoimmune diseases, such as systemic lupus erythematosus (SLE), type I diabetes, psoriasis, and vitiligo.[16–19] We examined *IFNB1* promoter activity induced by the c.2836G>A (p.Ala946Thr) polymorphism (rs1990760) identified in the GWASs. Although the c.2836G>A polymorphism partially activated the promoter activity, the induced activity was lower than those of the AGS-derived mutants. In addition, the dominantly inherited SLE mouse model in the ENU-treated mouse colony is reported to have the *Ifih1* mutation, c.2461G>A (p.Gly821Ser).[15] These observations suggest that *IFIH1* has strong association with various autoimmune diseases, especially SLE, which also has a type I interferon signature.[20] Because alteration of *TREX1* has been reported to cause AGS as well as SLE,[21] it seems quite plausible for *IFIH1* to also be involved in both AGS and SLE. Interestingly, all the individuals identified with *IFIH1* mutations had autoantibodies, suggesting the contribution of *IFIH1* mutations to autoimmune phenotypes.

To further delineate the functional consequences of the three *IFH1* mutations, we measured the ligand-specific *Ifnb* mRNA induction by stimulating *Ifih1*^{null} mouse embryonic fibroblasts (MEFs) reconstituted with retrovirus expressing the *IFIH1* mutants by an MDA5-specific ligand, encephalomyocarditis virus (EMCV).[22] None of the MEF cells expressing the three mutant *IFIH1* responded to the EMCV, which suggested that the MDA5 variants lacked the ligand-specific responsiveness. The response of the three AGS mutants against the MDA5-specific EMCV was similar to that of the p.Gly821Ser variant reported in the dominantly inherited SLE mouse model with type I interferon overproduction[15] (Figures 4 and S5).

During the revision of this manuscript, Rice et al. identified nine individuals with *IFIH1* mutations, including the c.2336G>A mutation we identified, in a spectrum of neuroimmunological features consistently associated with enhanced type I interferon states including AGS.[23] Although we agree that the *IFIH1* mutations cause constitutive type I interferon activation, Rice et al. show that the mutated MDA5 proteins maintain ligand-induced responsiveness, which was not the case in our study. Because we measured the ligand-specific responsiveness of MDA5 in different experimental conditions, further analysis remains to be performed to reveal the biochemical mechanism of interferon overproduction by the mutated MDA5.

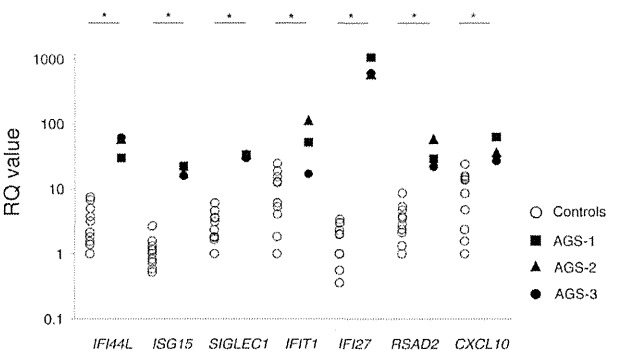

Figure 2. Quantitative RT-PCR of a Panel of Seven ISGs in PBMCs Obtained from the *IFIH1*-Mutated Individuals and Healthy Control Subject

qRT-PCR was performed as previously described.[15] The relative abundance of each transcript was normalized to the expression level of β-actin. Taqman probes used were the same as previous report,[14] except for *ACTB* (MIM 102630). Individual data were shown relative to a single calibrator (control 1). The experiment was performed in triplicate. Statistical significance was determined by Mann-Whitney U test, *$p < 0.05$.

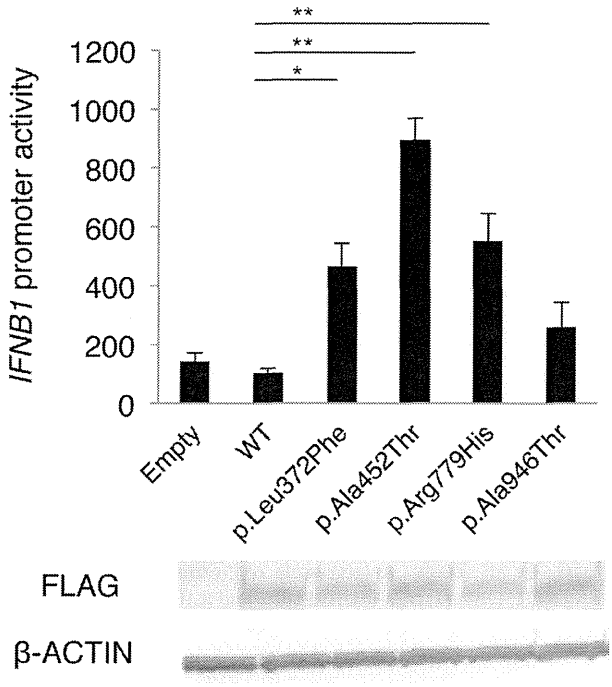

Figure 3. The Effects of the Three MDA5 Variants on *IFNB1* Expression
Huh7 cells were transfected with a reporter gene containing *IFNB1* promoter (p-55C1B Luc), an empty vector (BOS), and expression vectors for FLAG-tagged human wild-type *IFIH1*, c.2836G>A polymorphism (p.Ala946Thr) in the GWASs, and the identified *IFIH1* mutants. Luciferase activity was measured 48 hr after transfection, and the MDA5 protein accumulation was examined by immunoblotting as previously described.[15] FLAG indicates the accumulation of FLAG-tagged MDA5. Each experiment was performed in triplicate and data are mean ± SEM. Shown is a representative of two with consistent results. Statistical significance was determined by Student's t test. *$p < 0.05$, **$p < 0.01$.

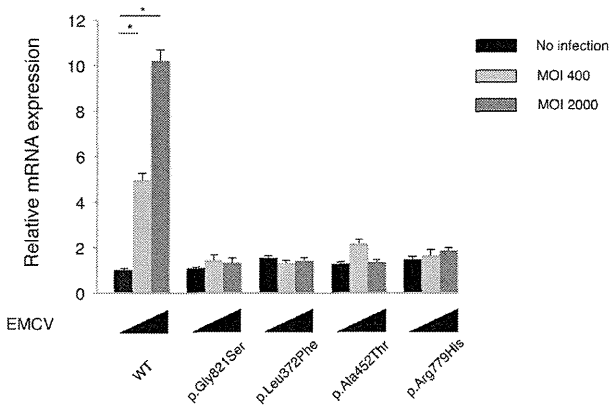

Figure 4. *Ifnb* mRNA Levels in *Ifih1*-Deficient MEFs Expressing *IFIH1* Mutants
The MEFs were infected with retroviruses encoding mouse wild-type *Ifih1*, mouse *Ifih1* with c.2461G>A (p.Gly821Ser) (RefSeq NM_027835.3) mutation, or the three AGS mutants of human *IFIH1*. At 48 hr after the retroviral infection, these MEFs were infected with indicated multiplicity of infection (MOI) of EMCV for 6 hr, and *Ifnb* mRNA levels were measured by qRT-PCR. The relative abundance of each transcript was normalized to the expression level of 18S ribosomal RNA. Data are shown as mean ± SEM of triplicate samples. Shown is a representative of two independent experiments. Statistical significance was determined by Student's t test, *$p < 0.001$. The expression of the retrovirally transduced FLAG-tagged constructs was confirmed by immunoblotting (Figure S5).

In conclusion, we identified mutations in *IFIH1* as a cause of AGS. The individuals with the *IFIH1* mutations showed encephalopathy typical of AGS as well as the type I interferon signature with autoimmune phenotypes, but lacked the chilblains. Further analysis remains to elucidate the mechanism of how the *IFIH1* mutations identified in AGS cause the type I interferon overproduction.

Supplemental Data

Supplemental Data include five figures and two tables and can be found with this article online at http://dx.doi.org/10.1016/j.ajhg.2014.06.007.

Acknowledgments

We are very grateful to Y. Takaoka (Kyoto University) and E. Abe (RIKEN Center for Integrative Medical Sciences) for their technical assistance on Sanger sequencing, to E. Hirano (Kyoto University) for her technical assistance on functional analyses of the AGS mutants, to M. Takazawa (Kazusa DNA Research Institute) for his contribution to exome data analysis, and to T. Taylor for his critical reading of the manuscript. This work was supported by the Platform for Drug Discovery, Informatics, and Structural Life Science from the Ministry of Education, Culture, Sports, Science and Technology, Japan. This work was supported by Grants-in-aid for Scientific Research from the Japanese Ministry of Health, Labor and Welfare and the Japanese Ministry of Education, Culture, Sports, Science, Technology (MEXT).

Received: March 1, 2014
Accepted: June 11, 2014
Published: July 3, 2014

Web Resources

The URLs for the data presented herein are as follows:

Burrows-Wheeler Aligner, http://bio-bwa.sourceforge.net/
ClustalW2, http://www.ebi.ac.uk/Tools/msa/clustalw2/
dbSNP, http://www.ncbi.nlm.nih.gov/projects/SNP/
EMDataBank, http://www.emdatabank.org/index.html
GATK, http://www.broadinstitute.org/gatk/
Human Genetic Variation Database (HGVD), http://www.genome.med.kyoto-u.ac.jp/SnpDB/
MutationTaster, http://www.mutationtaster.org/
Online Mendelian Inheritance in Man (OMIM), http://www.omim.org/
PolyPhen-2, http://www.genetics.bwh.harvard.edu/pph2/
PROVEAN, http://provean.jcvi.org/index.php
RCSB Protein Data Bank, http://www.rcsb.org/pdb/home/home.do
RefSeq, http://www.ncbi.nlm.nih.gov/RefSeq
SIFT, http://sift.bii.a-star.edu.sg/

References

1. Chahwan, C., and Chahwan, R. (2012). Aicardi-Goutieres syndrome: from patients to genes and beyond. Clin. Genet. *81*, 413–420.
2. Ramantani, G., Kohlhase, J., Hertzberg, C., Innes, A.M., Engel, K., Hunger, S., Borozdin, W., Mah, J.K., Ungerath, K., Walkenhorst, H., et al. (2010). Expanding the phenotypic spectrum of lupus erythematosus in Aicardi-Goutières syndrome. Arthritis Rheum. *62*, 1469–1477.
3. Orcesi, S., La Piana, R., and Fazzi, E. (2009). Aicardi-Goutieres syndrome. Br. Med. Bull. *89*, 183–201.
4. Rice, G., Patrick, T., Parmar, R., Taylor, C.F., Aeby, A., Aicardi, J., Artuch, R., Montalto, S.A., Bacino, C.A., Barroso, B., et al. (2007). Clinical and molecular phenotype of Aicardi-Goutieres syndrome. Am. J. Hum. Genet. *81*, 713–725.
5. Blau, N., Bonafé, L., Krägeloh-Mann, I., Thöny, B., Kierat, L., Häusler, M., and Ramaekers, V. (2003). Cerebrospinal fluid pterins and folates in Aicardi-Goutières syndrome: a new phenotype. Neurology *61*, 642–647.
6. Crow, Y.J., Hayward, B.E., Parmar, R., Robins, P., Leitch, A., Ali, M., Black, D.N., van Bokhoven, H., Brunner, H.G., Hamel, B.C., et al. (2006). Mutations in the gene encoding the 3′-5′ DNA exonuclease TREX1 cause Aicardi-Goutières syndrome at the AGS1 locus. Nat. Genet. *38*, 917–920.
7. Crow, Y.J., Leitch, A., Hayward, B.E., Garner, A., Parmar, R., Griffith, E., Ali, M., Semple, C., Aicardi, J., Babul-Hirji, R., et al. (2006). Mutations in genes encoding ribonuclease H2 subunits cause Aicardi-Goutières syndrome and mimic congenital viral brain infection. Nat. Genet. *38*, 910–916.
8. Rice, G.I., Bond, J., Asipu, A., Brunette, R.L., Manfield, I.W., Carr, I.M., Fuller, J.C., Jackson, R.M., Lamb, T., Briggs, T.A., et al. (2009). Mutations involved in Aicardi-Goutières syndrome implicate SAMHD1 as regulator of the innate immune response. Nat. Genet. *41*, 829–832.
9. Rice, G.I., Kasher, P.R., Forte, G.M., Mannion, N.M., Greenwood, S.M., Szynkiewicz, M., Dickerson, J.E., Bhaskar, S.S., Zampini, M., Briggs, T.A., et al. (2012). Mutations in ADAR1 cause Aicardi-Goutières syndrome associated with a type I interferon signature. Nat. Genet. *44*, 1243–1248.
10. Abe, J., Nakamura, K., Nishikomori, R., Kato, M., Mitsuiki, N., Izawa, K., Awaya, T., Kawai, T., Yasumi, T., Toyoshima, I., et al. (2014). A nationwide survey of Aicardi-Goutieres syndrome patients identifies a strong association between dominant TREX1 mutations and chilblain lesions: Japanese cohort study. Rheumatology *53*, 448–458.
11. Yoneyama, M., and Fujita, T. (2009). RNA recognition and signal transduction by RIG-I-like receptors. Immunol. Rev. *227*, 54–65.
12. Wu, B., Peisley, A., Richards, C., Yao, H., Zeng, X., Lin, C., Chu, F., Walz, T., and Hur, S. (2013). Structural basis for dsRNA recognition, filament formation, and antiviral signal activation by MDA5. Cell *152*, 276–289.
13. Berke, I.C., Yu, X., Modis, Y., and Egelman, E.H. (2012). MDA5 assembles into a polar helical filament on dsRNA. Proc. Natl. Acad. Sci. USA *109*, 18437–18441.
14. Rice, G.I., Forte, G.M., Szynkiewicz, M., Chase, D.S., Aeby, A., Abdel-Hamid, M.S., Ackroyd, S., Allcock, R., Bailey, K.M., Balottin, U., et al. (2013). Assessment of interferon-related biomarkers in Aicardi-Goutières syndrome associated with mutations in TREX1, RNASEH2A, RNASEH2B, RNASEH2C, SAMHD1, and ADAR: a case-control study. Lancet Neurol. *12*, 1159–1169.
15. Funabiki, M., Kato, H., Miyachi, Y., Toki, H., Motegi, H., Inoue, M., Minowa, O., Yoshida, A., Deguchi, K., Sato, H., et al. (2014). Autoimmune disorders associated with gain of function of the intracellular sensor MDA5. Immunity *40*, 199–212.
16. Smyth, D.J., Cooper, J.D., Bailey, R., Field, S., Burren, O., Smink, L.J., Guja, C., Ionescu-Tirgoviste, C., Widmer, B., Dunger, D.B., et al. (2006). A genome-wide association study of nonsynonymous SNPs identifies a type 1 diabetes locus in the interferon-induced helicase (IFIH1) region. Nat. Genet. *38*, 617–619.
17. Gateva, V., Sandling, J.K., Hom, G., Taylor, K.E., Chung, S.A., Sun, X., Ortmann, W., Kosoy, R., Ferreira, R.C., Nordmark, G., et al. (2009). A large-scale replication study identifies TNIP1, PRDM1, JAZF1, UHRF1BP1 and IL10 as risk loci for systemic lupus erythematosus. Nat. Genet. *41*, 1228–1233.
18. Strange, A., Capon, F., Spencer, C.C., Knight, J., Weale, M.E., Allen, M.H., Barton, A., Band, G., Bellenguez, C., Bergboer, J.G., et al.; Genetic Analysis of Psoriasis Consortium & the Wellcome Trust Case Control Consortium 2 (2010). A genome-wide association study identifies new psoriasis susceptibility loci and an interaction between HLA-C and ERAP1. Nat. Genet. *42*, 985–990.
19. Jin, Y., Birlea, S.A., Fain, P.R., Ferrara, T.M., Ben, S., Riccardi, S.L., Cole, J.B., Gowan, K., Holland, P.J., Bennett, D.C., et al. (2012). Genome-wide association analyses identify 13 new susceptibility loci for generalized vitiligo. Nat. Genet. *44*, 676–680.
20. Bennett, L., Palucka, A.K., Arce, E., Cantrell, V., Borvak, J., Banchereau, J., and Pascual, V. (2003). Interferon and granulopoiesis signatures in systemic lupus erythematosus blood. J. Exp. Med. *197*, 711–723.
21. Lee-Kirsch, M.A., Gong, M., Chowdhury, D., Senenko, L., Engel, K., Lee, Y.A., de Silva, U., Bailey, S.L., Witte, T., Vyse, T.J., et al. (2007). Mutations in the gene encoding the 3′-5′ DNA exonuclease TREX1 are associated with systemic lupus erythematosus. Nat. Genet. *39*, 1065–1067.
22. Kato, H., Takeuchi, O., Sato, S., Yoneyama, M., Yamamoto, M., Matsui, K., Uematsu, S., Jung, A., Kawai, T., Ishii, K.J., et al. (2006). Differential roles of MDA5 and RIG-I helicases in the recognition of RNA viruses. Nature *441*, 101–105.
23. Rice, G.I., del Toro Duany, Y., Jenkinson, E.M., Forte, G.M., Anderson, B.H., Ariaudo, G., Bader-Meunier, B., Baildam, E.M., Battini, R., Beresford, M.W., et al. (2014). Gain-of-function mutations in IFIH1 cause a spectrum of human disease phenotypes associated with upregulated type I interferon signaling. Nat. Genet. *46*, 503–509.

PEDIATRICS INTERNATIONAL Official Journal of the Japan Pediatric Society

Pediatrics International (2014) **56**, 605–629

Patient Reports

Munc13-4 deficiency with CD5 downregulation on activated CD8$^+$ T cells

Taizo Wada,[1] Takahiro Yasumi,[2] Tomoko Toma,[1] Masayuki Hori,[2] Sayaka Maeda,[2] Katsutsugu Umeda,[2] Toshio Heike,[2] Souichi Adachi,[2,3] Ikuya Usami[4] and Akihiro Yachie[1]

[1]*Department of Pediatrics, School of Medicine, Institute of Medical, Pharmaceutical and Health Sciences, Kanazawa University, Kanazawa,* [2]*Department of Pediatrics,* [3]*Human Health Sciences, Graduate School of Medicine, Kyoto University, Kyoto and* [4]*Department of Pediatrics, Hyogo Prefectural Tsukaguchi Hospital, Amagasaki, Japan*

Abstract Familial hemophagocytic lymphohistiocytosis (FHL) is characterized by uncontrolled activation of T cells and macrophages and hypercytokinemia. We have recently described a significant increase in a subpopulation of CD8$^+$ T cells with downregulation of CD5 during the acute phase of FHL type2 (FHL2; perforin deficiency), which declines after successful treatment, with a concomitant reduction in serum cytokine level. This unusual subset of CD8$^+$ T cells, however, has not been characterized in patients with other subtypes of FHL. Herein, we describe a patient with FHL3 (Munc13-4 deficiency) carrying compound heterozygous mutations in the *UNC13D* gene. He had high serum levels of pro-inflammatory cytokines and significantly increased activated CD8$^+$ T cells with downregulation of CD5 during the acute phase, similar to that found in FHL2. This immunophenotypic feature may serve as a useful marker of immune dysregulation in FHL3 in addition to FHL2.

Key words CD5, CD8$^+$ T cells, familial hemophagocytic lymphohistiocytosis, Munc13-4, UNC13D.

Hemophagocytic lymphohistiocytosis (HLH) is a systemic hyper-inflammatory disorder characterized by immune dysregulation and overproduction of cytokines.[1] Inherited forms of HLH include familial HLH (FHL), which is caused by genetic defects related to the granule-dependent cytotoxic pathway, and immunodeficiencies, such as X-linked lymphoproliferative syndrome. Mutations in the *PRF1*, *UNC13D*, *STX11*, and *STXBP2* genes lead to FHL type 2 (FHL2; perforin deficiency), FHL3 (Munc13-4 deficiency), FHL4 (syntaxin-11 deficiency), and FHL5 (Munc18-2 deficiency), respectively.[1] Recent nationwide surveys of FLH in Japan have indicated that the incidences of FHL2, FHL3 and FHL5 are 55%, 32% and 6%, respectively, and that no patients with FHL4 have been reported to date in Japan.[2] Perforin is an effector molecule for cytotoxicity that is present in cytolytic granules. Munc13-4, syntaxin-11 and Munc18-2 are involved in the intracellular trafficking and exocytosis of cytolytic granules.[1]

We have recently reported an increased subpopulation of activated CD8$^+$ T cells with downregulation of CD5 expression in patients with FHL2.[3] This unique immunophenotypic feature may serve as a useful marker of dysregulated T-cell activation and proliferation in FHL2.[3] Human CD5 is a membrane glycoprotein that belongs to the scavenger receptor cysteine-rich family of receptors, and is involved in the modulation of antigen-specific receptor-mediated activation and differentiation signals.[4] It is expressed on the majority of circulating T cells and a small proportion of B cells.[4] It has recently been reported that CD5 is recruited and co-localized with CD3 at the immunological synapse and inhibits T-cell receptor (TCR) signaling in T cells without interfering with immunological synapse formation.[5] In this report, we extended our previous observation[3] and investigated a patient with FHL3 who had downregulation of CD5 on activated CD8$^+$ T cells.

Correspondence: Taizo Wada, MD PhD, Department of Pediatrics, School of Medicine, Institute of Medical, Pharmaceutical and Health Sciences, Kanazawa University, 13-1 Takaramachi, Kanazawa 920-8641, Japan. Email: taizo@staff.kanazawa-u.ac.jp

Received 17 October 2013; revised 14 November 2013; accepted 17 December 2013.
doi: 10.1111/ped.12290

Case report

A 43-day-old Korean boy from non-consanguineous parents was hospitalized because of fever and petechiae. His family history was unremarkable. Due to a high copy number of cytomegalovirus (CMV) DNA in the peripheral blood and high serum titer of CMV IgM antibody, the patient was treated with CMV hyperimmune globulin, but he developed HLH at 55 days of age. His liver and spleen were palpable 4 cm and 6 cm below the subcostal margin, respectively. Laboratory tests were as follows: white blood cell count, 5260/μL; hemoglobin, 6.8 g/dL; and platelet count, 33×10^3/μL. The differential leukocyte count was 1% neutrophils, 94% lymphocytes, 4% atypical lymphocytes, and 1% monocytes. Other abnormal findings included mild liver dysfunction (aspartate aminotransferase, 74 IU/L), hypertriglyceridemia (238 mg/dL), and hyperferritinemia (7259 ng/mL). Profound hypercytokinemia was also noted: soluble interleukin (IL)-2 receptor, 16 380 IU/mL (normal, 145–519); IL-6, 9 pg/mL

(normal, <5); IL-18, 5600 pg/mL (normal, <500); tumor necrosis factor (TNF)-α, 40 pg/mL (normal, <10); soluble TNF receptor type 1, 10 600 pg/mL (normal, 484–1407); soluble TNF receptor type 2, 123 000 pg/mL (normal, 829–2262); and neopterin, 160 nmol/L (normal, 2–8). The natural killer cell (NK) activity was defective (5%; normal, 18–40%).

Immunophenotypic analysis of the lymphocyte showed an increased percentage of $CD3^+$ T cells (87.4%; normal, 72.3 ± 7.9%), the majority of which (88.6%) expressed the activation marker HLA-DR in the peripheral blood. The ratio of $CD4^+$ T (18.4%; normal, 53.1 ± 5.8%) to $CD8^+$ T cells (69.0%; normal, 17.3 ± 7.0%) was markedly inverted, and most of the $CD4^+$ and $CD8^+$ T cells expressed CD45RO. The percentage of $CD56^+$ NK cells was normal (6.5%). Flow cytometry for the TCR Vβ repertoire indicated polyclonal proliferation in both $CD4^+$ and $CD8^+$ T cells (data not shown). Based on our previous study,[3] we investigated whether an unusual subset of activated $CD8^+$ T cells with downregulation of CD5 expression was present in the patient. As shown in Figure 1, $CD4^+$ T cells exhibited normal expression of CD5. In contrast, a sizable proportion of CD5-negative cells were detected among the activated $CD8^+$ T cells. These findings prompted us to analyze perforin expression on flow cytometry in order to assess the possibility of FHL2.[3] NK cells from the patient, however, expressed perforin at a level similar to normal controls (data not shown).

We then performed a granule release assay.[6] As shown in Figure 2(a), the $CD56^+$ NK cells had diminished surface expression of CD107a relative to control NK cells after stimulation with K562 human erythroleukemia cells, indicating impaired lysosomal degranulation. Therefore, expression of Munc13-4, syntaxin-11, and Munc18-2 was evaluated in platelets on western blot analysis.[6] We were able to clearly show that Munc13-4 was not detectable in the patient (Fig. 2b). To identify the mutations responsible for FHL3, direct sequence analysis of the *UNC13D* gene was performed.[6] The patient was a compound heterozygote bearing two different intronic mutations (Fig. 3). One was a splice site mutation, c.754-1G>C (IVS9-1G>C); the other was a deep intronic mutation in intron 1, c.118-308C>T. Both mutations have been commonly reported in Korean patients with FHL3.[7]

The patient was treated with the HLH-2004 treatment protocol, including dexamethasone, cyclosporine A and etoposide, as well as plasmapheresis for 3 days and ganciclovir. After the diagnosis of FHL3 was confirmed molecularly, he underwent cord blood stem cell transplantation at the age of 4 months, and is alive with no evidence of disease at the age of 11 months.

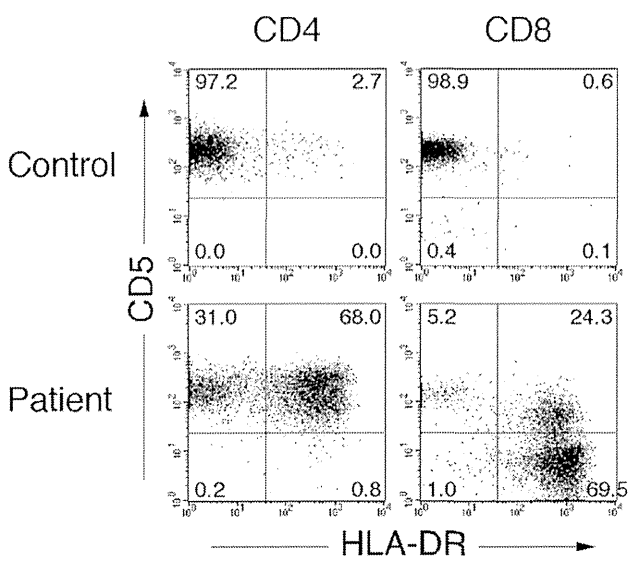

Fig. 1 Expression of CD5 and HLA-DR on the $CD4^+$ and $CD8^+$ T cells. Peripheral blood was obtained from a healthy adult volunteer and the patient. The percentage of cells gated in each region is shown.

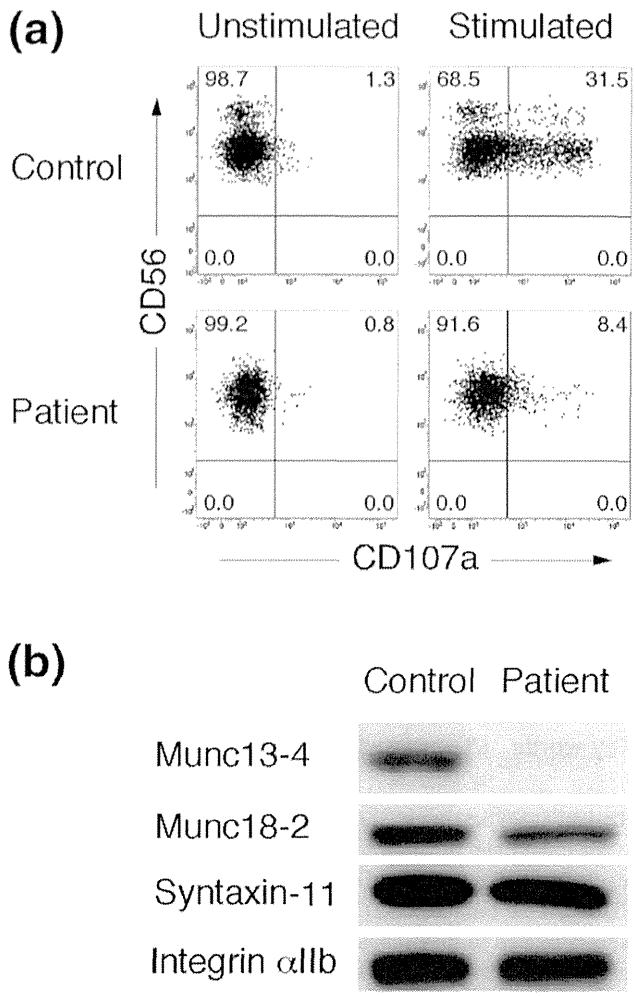

Fig. 2 (a) Granule release assay. Peripheral blood mononuclear cells from a control subject and the patient were co-cultured with K562 cells for 2 h. Cells were stained with anti-CD3, anti-CD56, and anti-CD107a antibodies. The expression of CD107a in the $CD3^-$ $CD56^+$ natural killer cells is shown. (b) Western blot analysis of Munc13-4, Munc18-2 and syntaxin-11 done using platelet lysates. Immunoblotting with anti-integrin αIIb is shown as a loading control.

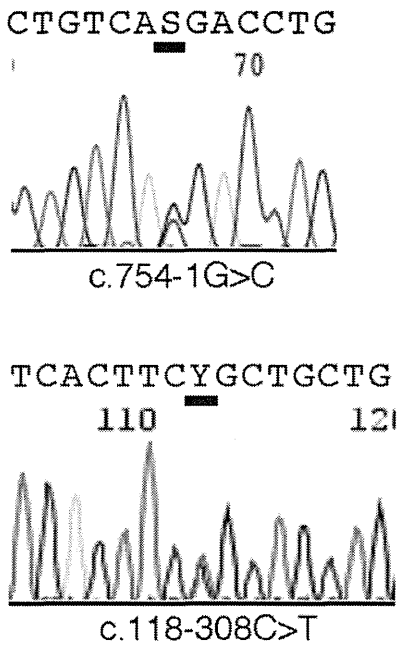

Fig. 3 Analysis of *UNC13D* mutations. Direct sequencing of the *UNC13D* gene was performed using an automated sequencer. Bar, location of the mutations.

Discussion

Familial hemophagocytic lymphohistiocytosis is a rare autosomal recessive disorder caused by genetic defects related to granule-dependent cytotoxicity and is characterized by uncontrolled proliferation of activated macrophages and T cells with overproduction of pro-inflammatory cytokines.[1] We have recently described the downregulation of CD5 expression on activated CD8+ T cells during the acute phase of FHL2, which may serve as a useful marker of dysregulated T-cell activation and proliferation in FHL2. The immunophenotypic features of T cells in other subtypes of FHL, however, have not been fully characterized. In addition, downregulation of CD5 is likely a general consequence of the dysregulated proliferation of CD8+ T cells. The appearance of such unique cells has been reported in patients with Epstein–Barr virus-HLH, allogeneic bone marrow transplantation, HIV-1 infection, acute herpes virus infections and peripheral T-cell neoplasm.[8] We, therefore, continue to investigate CD5 expression in children with a suspected diagnosis of HLH.

In the present study, we describe a case of FHL3 that was triggered by primary CMV infection. During the acute phase, the patient had marked hypercytokinemia and proliferation of CD8+ T cells. More importantly, a significant increase in the subpopulation of activated CD8+ T cells with downregulation of CD5 expression was demonstrated in the patient. These findings are similar to those of FHL2.[3] While the mechanism underlying downregulation of CD5 on activated CD8+ T cells remains to be elucidated, it is tempting to speculate that patients with any of the FHL subtypes other than FHL2 might also have downregulation of CD5 on activated CD8+ T cells during the acute phase. Because CD5-negative T cells have been shown to become hyperresponsive to TCR stimulation in CD5-deficient mice,[9] downregulation of CD5 might contribute to the uncontrolled activation and proliferation of CD8+ T cells in FHL. It is unknown whether CD8+ T cells from other HLH patients have similar profiles during the acute phase. Further investigations are required to address these issue.

Recently Murata *et al.* reported that Munc13-4, syntaxin-11, and Munc18-2 were all abundantly expressed in platelets, indicating the usefulness of platelet proteins for the screening of FHL.[6] Indeed, the present patient was successfully screened for FHL3–FHL5 on western blot analysis of platelets after the CD107a granule release assay. Genetic analysis is often labor-intensive and time-consuming. In addition, a deep intronic mutation similar to c.118-308C>T in the *UNC13D* gene that has been shown to selectively impair gene transcription and abolish Munc13-4 expression could be a disease-causing mutation.[10] Therefore, the present screening methods, as well as flow cytometry detection of intraplatelet Munc-13-4 protein, represent valuable tools for the identification of the FHL subtypes before performing mutation analysis.

In conclusion, this is an additional example of downregulation of CD5 on activated CD8+ T cells, further supporting its potential as a useful marker of dysregulated T-cell activation and proliferation in FHL3 in addition to FHL2.

Acknowledgments

We thank Ms Harumi Matsukawa and Ms Shizu Kouraba for their excellent technical assistance. This work was supported by a Grant-in-Aid for Scientific Research from the Ministry of Education, Culture, Sports, Science and Technology of Japan; and a grant from the Ministry of Health, Labour, and Welfare of Japan, Tokyo. The authors declare no conflicts of interest.

References

1 Usmani GN, Woda BA, Newburger PE. Advances in understanding the pathogenesis of HLH. *Br. J. Haematol.* 2013; **161**: 609–22.
2 Nagai K, Yamamoto K, Fujiwara H *et al.* Subtypes of familial hemophagocytic lymphohistiocytosis in Japan based on genetic and functional analyses of cytotoxic T lymphocytes. *PLoS ONE* 2010; **5**: e14173.
3 Wada T, Sakakibara Y, Nishimura R *et al.* Down-regulation of CD5 expression on activated CD8+ T cells in familial hemophagocytic lymphohistiocytosis with perforin gene mutations. *Hum. Immunol.* 2013; **74**: 1579–85.
4 Lozano F, Simarro M, Calvo J *et al.* CD5 signal transduction: Positive or negative modulation of antigen receptor signaling. *Crit. Rev. Immunol.* 2000; **20**: 347–58.
5 Brossard C, Semichon M, Trautmann A, Bismuth G. CD5 inhibits signaling at the immunological synapse without impairing its formation. *J. Immunol.* 2003; **170**: 4623–9.
6 Murata Y, Yasumi T, Shirakawa R *et al.* Rapid diagnosis of FHL3 by flow cytometric detection of intraplatelet Munc13-4 protein. *Blood* 2011; **118**: 1225–30.
7 Seo JY, Song JS, Lee KO *et al.* Founder effects in two predominant intronic mutations of UNC13D, c.118-308C>T and c.754-1G>C underlie the unusual predominance of type 3 familial hemophagocytic lymphohistiocytosis (FHL3) in Korea. *Ann. Hematol.* 2013; **92**: 357–64.

8 Toga A, Wada T, Sakakibara Y *et al.* Clinical significance of cloned expansion and CD5 down-regulation in Epstein-Barr virus (EBV)-infected CD8+ T lymphocytes in EBV-associated hemophagocytic lymphohistiocytosis. *J. Infect. Dis.* 2010; **201**: 1923–32.
9 Tarakhovsky A, Kanner SB, Hombach J *et al.* A role for CD5 in TCR-mediated signal transduction and thymocyte selection. *Science* 1995; **269**: 535–7.
10 Meeths M, Chiang SC, Wood SM *et al.* Familial hemophagocytic lymphohistiocytosis type 3 (FHL3) caused by deep intronic mutation and inversion in UNC13D. *Blood* 2011; **118**: 5783–93.

Coexistence of neuroblastoma detected on staging of Langerhans cell histiocytosis

Tadashi Shiohama,[1] Hidemasa Ochiai,[1] Tomoro Hishiki,[2] Hideo Yoshida[2] and Yoichi Kohno[1]
Departments of [1]Pediatrics, and [2]Pediatric Surgery, Chiba University Graduate School of Medicine, Chiba, Japan

Abstract Langerhans cell histiocytosis (LCH) is a rare proliferative disease accompanied by the accumulation of pathological Langerhans cells, which often spreads into multi-site and multi-organ systems. We here describe a girl with a history of Kawasaki disease and cervical lymphadenopathy who presented with occipital LCH. Adrenal tumor was detected on staging evaluation of LCH and was diagnosed as neuroblastoma on resection using laparoscopic surgery. Neither tumor relapsed following chemotherapy for LCH and resection of neuroblastoma. Although LCH often spreads into multi-organ lesions, invasive biopsy may be needed for tumors with atypical localization for LCH in consideration of the synchronous occurrence of malignancies.

Key words Kawasaki disease, Langerhans cell histiocytosis, laparoscopy, lymphadenopathy, neuroblastoma.

Langerhans cell histiocytosis (LCH) is a rare proliferative disease accompanied by the accumulation of pathological Langerhans cells. Its clinical manifestations have been recognized as existing along a spectrum that may involve a single site, multiple sites in a single organ system, or multiple organ systems. Stratifying patients based on their position on the spectrum has proven useful in determining prognosis and planning suitable therapy.[1]

Neuroblastoma (NB) is the most common extracranial solid tumor that occurs in childhood. NB is a disease of the sympathicoadrenal lineage of the neural crest; therefore, it can develop anywhere in the sympathetic nervous system, with a predilection for the adrenal glands.[2]

We here present the case of a girl with co-occurrence of stage 1 NB detected on staging evaluation of LCH. Although LCH may involve a multi-organ system, we need to consider the possibility of the coexistence of malignancies in the staging of LCH.

Case report

A previously healthy girl was admitted to hospital for Kawasaki disease (KD) at 18 months old. She was successfully treated with i.v. high-dose immunoglobulin with oral aspirin and recovered without coronary complications. Abdominal ultrasonography was not performed at that time. At 2 years 4 months old, she presented with bilateral lymphadenopathy, which resolved without therapy.

At 3 years old, she entered hospital for evaluation of an occipital mass, which had presented 3 months before. Skull X-ray indicated a 2 cm punched-out lesion. Cranial magnetic resonance imaging showed an intracranial-extending soft-tissue mass adjacent to the sagittal sinus (Fig. 1a), without invasion into the central nervous system. Excisional biopsy specimen confirmed the diagnosis of LCH on histological analysis including S100 and CD1a stains. Computed tomography (CT) to define organ involvement showed a right adrenal tumor (2.5 cm × 3.0 cm). The tumor presented isointensity with the liver on T1-weighted imaging, high intensity on T2-weighted imaging, and Gd enhancement (Fig. 1b). The tumor had high ^{67}Ga scintigraphy activity and positive ^{99m}Tc HMDP uptake on bone scintigraphy. Urinary homovanillic acid (HVA) was 3.27 mg/g Cr (normal, 3.5–11.9 mg/g Cr); urinary vanillylmandelic acid (VMA), 2.63 mg/g Cr (normal, 4.1–19.3 mg/g Cr); and serum neuron-specific enolase, 15.73 ng/mL (normal, 0–10 ng/mL).

Because the localization of LCH uncharacteristically involved the adrenal glands, the right adrenal tumor was resected using laparoscopic surgery for additional diagnosis. The histological diagnosis was NB, differentiating, according to International Neuroblastoma Pathology Classification. The tumor sample

Correspondence: Tadashi Shiohama, MD PhD, Department of Pediatrics, Chiba University Graduate School of Medicine, 1-8-1 Inohana, Chuo-ku, Chiba-shi, Chiba 260-8670, Japan. Email: asuha_hare@yahoo.co.jp

Received 27 May 2013; revised 12 October 2013; accepted 19 December 2013.
doi: 10.1111/ped.12292